

1 Cite this article as:

2 G. Battaglia, L. Gurreri, M. Ciofalo, A. Cipollina, I. D. L. Bogle, A. Pirrotta, G. Micale, A 2-D  
3 model of electro dialysis stacks including the effects of membrane deformation, *Desalination*, 500  
4 (2021) 114835.

5 <https://doi.org/10.1016/j.desal.2020.114835>.

## 6 **A 2-D model of electro dialysis stacks including the effects of** 7 **membrane deformation**

8 *Giuseppe Battaglia*<sup>1</sup>, *Luigi Gurreri*<sup>1,\*</sup>, *Michele Ciofalo*<sup>1</sup>, *Andrea Cipollina*<sup>1</sup>, *I. David L. Bogle*<sup>2</sup>,  
9 *Antonina Pirrotta*<sup>1</sup>, *Giorgio Micale*<sup>1</sup>

10 <sup>1</sup> *Dipartimento di Ingegneria, Università degli Studi di Palermo, Viale delle Scienze ed. 6,*  
11 *90128 Palermo, Italy.*

12 <sup>2</sup> *Centre for Process Systems Engineering, Department of Chemical Engineering, University*  
13 *College London, Torrington Place, London WC1E 7JE, UK*

14 *\*Corresponding author. E-mail address: [luigi.gurreri@unipa.it](mailto:luigi.gurreri@unipa.it) (L. Gurreri)*

### 16 **ABSTRACT**

17 Membrane-based processes have gained a relevant role in many engineering applications.  
18 Much effort has been devoted to thoroughly understand the fundamental phenomena behind  
19 them. However, membrane deformation has been taken into consideration only recently,  
20 although much evidence has shown its impacts in many applications. This work presents a novel  
21 2-D, multi-scale, semi-empirical process model able to predict the behaviour and the  
22 performance of Electro dialysis (ED) systems in cross-flow configurations in the presence and  
23 absence of local membrane deformations. The model exploits the results and the simulation  
24 approaches of previous fluid-structure investigations performed by the authors. Low-scale  
25 numerical simulations are coupled with a high-scale model to predict the redistribution of  
26 channel height, flow rate, friction coefficient and Sherwood number in ED stacks caused by  
27 local membrane deformations. Finally, salt and water fluxes, mass balances and  
28 electrochemical quantities are computed to assess the performances of cross-flow ED stacks.  
29 Different test cases have been simulated for the desalination of seawater by two-stage ED.  
30 Interestingly, membrane deformation is found to reduce, albeit slightly, the energy  
31 consumption. More pronounced effects are expected if thinner or less stiff membranes are used.

32  
33 **Keywords**

34 Ion exchange membrane, profiled membrane, transmembrane pressure, membrane deflection,  
35 desalination

36

## 37 **1. Introduction**

38 In the last 60 years, membrane-based separation processes have been established as  
39 promising technologies in a broad range of applications, e.g. potable water production from  
40 seawater and brackish water [1,2], wastewater treatment [3,4], food engineering [5], energy  
41 production from non-conventional sources [6,7] and biomedical applications [8]. The key  
42 components of these processes are the membranes, which allow the permeation of a chemical  
43 species to be controlled [9]. In recent years, much effort has been devoted to improve membrane  
44 properties, allowing membrane-based processes to become increasingly competitive in all their  
45 fields of application.

46 In this context, many studies have been focused on the better understanding of the  
47 fundamental physical, thermo-dynamical and electrochemical phenomena characterizing the  
48 functioning of many membrane processes. However, only recently the mechanical behaviour  
49 of membranes has been taken into account. From a mechanical point of view, membranes are  
50 very thin elements, whose mechanical response can be studied as that of thin plates, having no  
51 bending stiffness, undergoing large deflections. Membranes are mainly made of polymeric  
52 materials, which have low mechanical properties in terms of Young modulus and yield stress.  
53 This makes the membrane prone to deform when subjected to even small loads. Moreover, due  
54 to their small elastic region (low yield stress), the membranes' deformation may likely be  
55 irreversible.

56 In membrane-based processes, a pressure difference between two solutions, flowing in two  
57 fluid channels separated by a membrane, may arise. This pressure difference is referred to as  
58 transmembrane pressure, TMP. Experimental evidence has shown the significant effects of  
59 TMP in many membrane technologies, as briefly reviewed here below.

60 A water flux decline was detected in Reverse Osmosis (RO) seawater treatment working at  
61 6900 kPa [10]. The authors attributed this phenomenon also to membrane deformation, which  
62 causes membranes to be squeezed through the permeate spacer thus leading to a reduction of  
63 the membrane active area.

64 In Forward Osmosis, the effects of membrane draw channel contraction caused by  
65 membrane deformation have been investigated experimentally and numerically in a system  
66 equipped with a dot geometry spacer in the draw channel [11]. Membrane deformation was not  
67 simulated, but ellipsoidal-shaped membrane deformation was assumed to occur through the

68 dot-spacer supports. The membrane was found to stretch from 0 to 67.7% of the nominal  
69 channel height under a TMP between 0 and 145 kPa. Shear rates along the membrane surface  
70 and fluid flow regime in deformed channels were also studied by performing CFD simulations  
71 showing complex effects of membrane deformation on them.

72 In Assisted Forward Osmosis, two different permeate spacer types were investigated to  
73 address membrane deformation issues [12]: (1) a commercial 1.2 mm diamond-type mesh  
74 spacer and (2) a finer porous frit support. Hydraulic pressure impact was investigated in a  
75 pressure range between 200 and 600 kPa. Using the frit support, pure water permeability and  
76 salt permeability were almost constant in all the pressure range investigated, while they both  
77 increased when the system was equipped with the commercial spacer. Digital images of the  
78 membranes, taken after tests at 600 kPa, clearly showed that this behaviour was mainly related  
79 to membrane deformation.

80 Membrane deformation phenomena have also been largely reported in Pressure Retarded  
81 Osmosis (PRO) [13–21]. The most appropriate PRO setup, to be used for high pressure  
82 operations, was investigated in [16]. Results showed that, when a critical limit pressure of 5520  
83 kPa was exceeded, the water flux drastically increased, indicating excessive membrane  
84 deformation. In addition, results suggested that the use of small opening spacers, although  
85 leading to higher shadow effects, guarantees a better mechanical stability of the membranes  
86 avoiding their collapse. Similar findings were also shown in [17,18] working at lower pressures  
87 of 2000-2500 kPa.

88 In pressure-retarded membrane distillation, the performance of a system was investigated  
89 in a pressure range between 0 and 1000 kPa using tricot-type spacers with small openings (<  
90 0.35 mm) [22]. No power output and a considerable water vapour flux reduction were detected  
91 working at a pressure higher than 200 kPa. Concave and convex deformed shapes of the  
92 membranes were optically observed. Further analysis also showed that coarse net-type spacers  
93 (openings > 0.35 mm) caused much more severe membrane deformation leading to membrane  
94 damage even at pressure values lower than 200 kPa.

95 In permeate gap membrane distillation with simultaneous fresh water and energy  
96 production, the performance of a unit using two different membranes was investigated adopting  
97 an assembled package layers of diamond shape mesh plastic spacer and stainless steel woven  
98 mesh with 0.154 mm aperture [23]. The membranes tested could only withstand pressures lower  
99 than 200 kPa and the system produced a much lower power density than that theoretically  
100 predicted.

101 In many other membrane-based processes, membrane deformation issues have also been  
102 reported, e.g. liquid-to-air membrane energy exchangers [24] and proton exchange membranes  
103 for fuel cells [25,26].

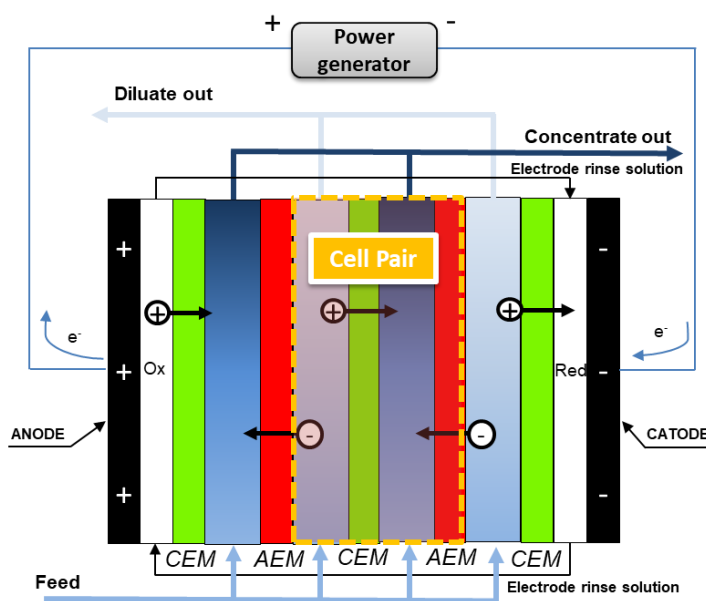
104 This short literature review clearly shows that membrane deformation phenomena may  
105 have a significant impact on the performances of membrane-based processes.

106 In electro-membrane processes, such as Electrodialysis (ED) and Reverse Electrodialysis  
107 (RED), trans-membrane pressures are usually smaller than those considered in the above  
108 studies, and are mainly caused by the frictional losses occurring in the fluids flowing on the  
109 opposite sides of each membrane. However, many practical (R)ED working conditions could  
110 lead to non-negligible TMP values. Novel ED stack configurations have been investigated in  
111 [27] in order to reduce the energy demand of ED stacks for brackish water desalination. Lab-  
112 scale experiments performed using parallel- and counter- flow ED stacks showed that counter-  
113 flow configuration allowed a 10-30% reduction of the energy consumption with respect to that  
114 of the parallel-flow arrangement. TMP values lower than 30 kPa were measured during the  
115 experiments. In RED applications, the power generation performance of a bench-scale RED  
116 stack (40 m<sup>2</sup>) has been investigated in [28]. The RED stack was fed using natural seawater RO  
117 brine and sewage-treated water (STW). Results showed that at a given STW flow rate, the RED  
118 stack was able to produce higher gross power densities as the RO brine flow rates increased.  
119 The authors did not give an estimation of the TMP values in the stack; however, they attributed  
120 the increase of the gross power densities to a possible contraction of the STW channel, which  
121 caused a reduction of the Ohmic stack resistance, when the RO brine solution was pumped at  
122 higher flow rate than that of the STW solution. Many other practical (R)ED working conditions  
123 where non-negligible TMP values could arise have been also identified by the present authors  
124 in [29–31]. In this context, the present work aims at presenting a comprehensive process model  
125 tool, which can be used for the design of an ED stack (and of a RED stack, just making a few  
126 adjustments) taking into account also membrane deformation phenomena.

## 127 128 **1.1 Modelling of Electrodialysis systems**

129 Electrodesialysis is an electrochemical process in which an external electric potential is used  
130 as the driving force [32]. ED has been established to be a promising technology for drinking  
131 water production through the desalination of brackish water or even seawater sources. In an ED  
132 stack, a couple of anion and cation exchange membranes (*AEMs* and *CEMs*) are alternatively  
133 piled and separated by means of net-spacers or membrane built-in profiles, which define the  
134 fluid channels where solutions flow. When the external potential is applied to the system, an

135 ionic current is induced, leading ions to migrate from one solution to the adjacent ones through  
 136 the membranes. In the process, ion concentration increases in one solution (concentrate  
 137 solution, *CON*), while it decreases in the other one (diluate solution, *DIL*). A couple of an *AEM*  
 138 and a *CEM* together with one *CON* and one *DIL* channel form the so called “cell pair”, which  
 139 represents the fundamental repetitive unit of an ED stack. ED stacks can be made from a few,  
 140 e.g. 10-50 at lab scale, to hundreds of cell pairs, e.g. 500 at industrial scale. Electrode  
 141 compartments are placed at the two external sides of a stack to allow the conversion of the  
 142 external electric current into ion fluxes in the stack via redox reactions. A schematic  
 143 representation of an ED stack is shown in Figure 1.



144  
 145 **Figure 1.** Schematic representation of an Electrodialysis stack. Adapted from [2].  
 146

147 Many numerical and theoretical models have been developed to study and design of ED  
 148 systems spanning from very simplified to advanced theoretical models [2]. In particular,  
 149 simplified models are based on many assumptions and usually employ a lumped parameters  
 150 approach. They have been proposed for a preliminary design of specific ED stacks relying on  
 151 experimentally determined parameters [33,34].

152 Conversely, advanced models give a more accurate description of the functioning of a  
 153 system by taking into account spatial effects and non-ideal phenomena. They can be divided  
 154 into two sub-categories: theoretical and semi-empirical models.

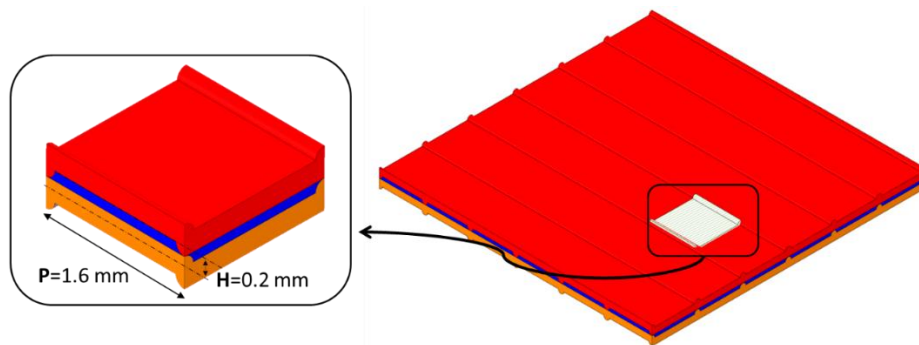
155 Theoretical models aim at describing ED, but also RED, phenomena based on rigorous  
 156 theories by solving a complex set of equations [35–39] (i.e. the Nernst-Planck equation, or even  
 157 the more complex Stefan-Maxwell equations). However, they require a large amount of

158 computational power and several thermodynamic and electrochemical parameters which are  
159 difficult to be found, and their application is usually limited to the simulation of a small-scale  
160 portion of a real stack.

161 Semi-empirical models, instead, aim at describing a (R)ED stack at its whole scale, taking  
162 spatial effects into account, but have to use empirical information for membrane properties (e.g.  
163 salt permeability, ohmic resistance, osmotic permeability, etc.) and for local hydraulic and mass  
164 transfer characteristics of the channels (permeability, limiting current density, Sherwood  
165 number) [40–43]. As an alternative to empirical input, these models can use correlation  
166 obtained from the small-scale simulation of specific phenomena, e.g. by means of  
167 Computational Fluid Dynamics [44–48] (multi-scale approach).

168 As far as ED/RED modelling is concerned, with a few exceptions [49,50], most of the  
169 proposed semi-empirical models are one-dimensional. A 2-D approach allows the study of more  
170 stack configurations (such as the cross-flow one) besides the classical parallel- and counter-  
171 flow arrangements. The present work introduces a novel 2-D semi-empirical, multi-scale model  
172 to address the performance of ED stacks in cross-flow configurations with and without  
173 membrane deformation phenomena.

174 In regard to the membrane deformation treatment, a multi-scale modelling approach is  
175 exploited. In previous work [29,30] coupled mechanical and fluid dynamics simulations were  
176 conducted using a Finite Element (FE) / Finite Volume (FV) method as implemented in the  
177 commercial software Ansys Mechanical® and Ansys CFX®. At this stage, the study was  
178 conducted at the low scale of a periodic repetitive unit of a fluid channel bounded by two  
179 membranes (unit cell), shown in Figure 2. In particular, results were obtained for Overlapped  
180 Crossed Filament (OCF) profiled membranes having a pitch  $P$  (distance between two  
181 consecutive filaments) of 1.6 mm and a channel height  $H$  of 0.2 mm, leading to a  $P/H$  ratio  
182 equal to 8.



183  
184 **Figure 2.** Sketch of a channel bounded by two Overlapped Crossed Filament (OCF) profiled membranes  
185 with  $P/H = 8$ . The detail of a unit cell is illustrated on the left. Adapted from [29].

186

187 A one-way fluid-structure approach was employed to study the effect of membrane  
188 deformation due to the action of an imposed TMP (simulated as the difference between external  
189 and internal pressure) varying between -40 kPa and 40 kPa. Results were the fluid dynamics  
190 and mass transport properties of the corresponding deformed fluid channel for each deformed  
191 configuration simulated.

192 Based on these results, a full two-way fluid-structure interaction model was developed in  
193 [31] to assess membrane deformation effects on the flow re-distribution at the higher scale of a  
194 whole cell pair. This was carried out by developing an original closed-loop iterative algorithm,  
195 which takes into account the local change of the channel's hydraulic permeability as a function  
196 of the local transmembrane pressure (TMP), which, in its turn, varies with the local flow rate  
197 and eventually with the channel's permeability. No effects on mass transfer rates were  
198 considered in [31].

199 The present work adds the last piece of the puzzle by integrating the approach in [31] with  
200 a 2-D modelling of the main physical and electrochemical phenomena of the ED process,  
201 including deformation effects on mass transfer. The result is a comprehensive modelling tool,  
202 which encloses most of the previous modelling approaches to assess the performance of ED  
203 stacks in terms of energy requirements and product quality either in the presence or in the  
204 absence of membrane deformation.

205

## 206 **2. Modelling**

207 The present model simulates transport and electrochemical phenomena occurring in ED  
208 stacks, computing the distribution of the main variables in a cell pair (assumed to be  
209 representative of the whole stack) and assessing the process performance, e.g. the energy  
210 consumption. As mentioned before, to describe the effect of membrane deformation a multi-  
211 scale approach is employed. Specifically:

- 212 (i) At the lowest scale, FE-FV simulations provide channel deformation, friction  
213 coefficients and Sherwood numbers as functions of the transmembrane pressure (TMP)  
214 in the fluid channels.
- 215 (ii) At the higher scale of the cell pair, the equations expressing mass balances, transport  
216 phenomena, solutions and membrane properties are solved, taking into account (if  
217 required) the local flow redistribution in the channels due to local membrane  
218 deformations.
- 219 (iii) Finally, at the highest scale of the stack, the ED performance is predicted for any  
220 number of cell pairs, taking into account the resistance of the electrode compartments.

221 The main model assumptions are:

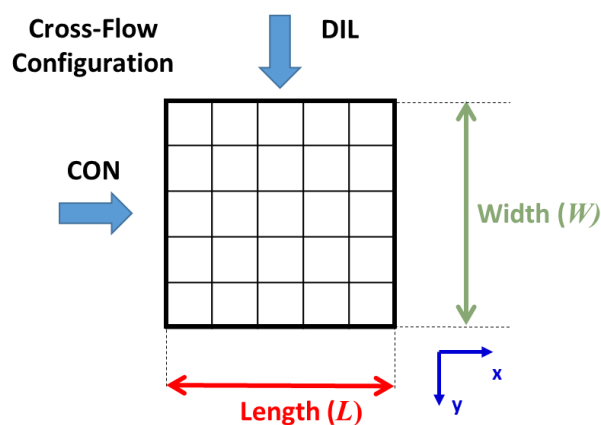
- 222 1. Each channel is simulated as a porous isotropic medium with locally variable porosity
- 223  $\varepsilon$  and hydraulic permeability  $K$ ;
- 224 2. binary electrolyte solutions (specifically, NaCl) are considered;
- 225 3. steady-state regime is assumed;
- 226 4. all cell pairs behave in the same way;
- 227 5. empirical expressions for the limiting current density are not used;
- 228 6. parasitic currents are not considered;
- 229 7. manifolds are not included in the model.

230 In regard to assumption 5, it should be observed that, in the absence of specific correlations for  
231 the limiting current density, the model allows the current density to grow until either  
232 concentration at the diluate-membrane interfaces becomes zero. It is known that this condition  
233 (diffusion limited current density) is never actually attained in real ED, and that empirical  
234 correlations are required to predict more realistic limiting current density values.

235

## 236 2.1 Mass balances and fluxes in an ED stack

237 In a two-dimensional approach, the distribution of all variables is evaluated over the length  
238 ( $L$ ) and width ( $W$ ) of a channel. Considering a cross-flow arrangement, as shown in Figure 3,  
239 the concentrate solution ( $CON$ ) may be assumed to flow (on average) from left to right, parallel  
240 to the  $x$ -axis, while the dilute solution ( $DIL$ ) may be assumed to flow (on average) from top to  
241 bottom, parallel to the  $y$ -axis.



242

243 **Figure 3.** Computational domain of the developed model for a 2-D cross-flow configuration.

244

245 Under the assumption of constant density solutions, differential mass balances for the salt  
246 and water species in the concentrate and diluate channels can be written as:

$$247 \quad \frac{\partial U_x^{CON}(x, y) C^{CON}(x, y)}{\partial x} + \frac{\partial U_y^{CON}(x, y) C^{CON}(x, y)}{\partial y} = + \frac{1}{H} N_{SALT}^{TOT}(x, y); \quad (1)$$

$$248 \quad \frac{\partial U_x^{CON}(x, y)}{\partial x} + \frac{\partial U_y^{CON}(x, y)}{\partial y} = + \frac{1}{H} J_W^{TOT}(x, y); \quad (2)$$

$$249 \quad \frac{\partial U_x^{DIL}(x, y) C^{DIL}(x, y)}{\partial x} + \frac{\partial U_y^{DIL}(x, y) C^{DIL}(x, y)}{\partial y} = - \frac{1}{H} N_{SALT}^{TOT}(x, y); \quad (3)$$

$$250 \quad \frac{\partial U_x^{DIL}(x, y)}{\partial x} + \frac{\partial U_y^{DIL}(x, y)}{\partial y} = - \frac{1}{H} J_W^{TOT}(x, y); \quad (4)$$

251 where:

- 252 •  $U_x^{SOL}(x, y)$  and  $U_y^{SOL}(x, y)$  are the local superficial velocities (in m/s) along  $x$  and  $y$  in
- 253 the channel  $SOL$ , which can be either  $CON$  (concentrate channel) or  $DIL$  (dilute
- 254 channel). They represent averages over the nominal (undeformed) channel thickness  $H$ ;
- 255 •  $C^{SOL}(x, y)$  is the local salt concentration (also averaged over the channel thickness  $H$ )
- 256 in the  $SOL$  ( $CON$  or  $DIL$ ) channel, in mol/m<sup>3</sup>;
- 257 •  $N_{SALT}^{TOT}(x, y)$  is the local transmembrane molar salt flux, summed over both membranes,
- 258 taken in absolute value and expressed in mol/(m<sup>2</sup> s).
- 259 •  $J_W^{TOT}(x, y)$  is the local transmembrane volumetric water flux, summed over both
- 260 membranes, taken in absolute value and expressed in m<sup>3</sup>/(m<sup>2</sup> s), i.e. in m/s.

261

262 As far as the total transmembrane water flux is concerned, it can be expressed as the sum

263 of two terms:

$$264 \quad J_W^{TOT}(x, y) = J_W^{OSM}(x, y) + J_W^{E.OSM}(x, y) \quad (5)$$

265 accounting for osmotic and electro-osmotic transport mechanisms, respectively.

266 The osmotic term,  $J_W^{OSM}(x, y)$ , describes the water transport due to the interfacial osmotic

267 pressure gradient between concentrate and dilute solutions across the membranes:

$$268 \quad J_W^{OSM}(x, y) = L_{p,AEM} \left[ \pi_{AEM}^{CON}(x, y) - \pi_{AEM}^{DIL}(x, y) \right] +$$

$$+ L_{p,CEM} \left[ \pi_{CEM}^{CON}(x, y) - \pi_{CEM}^{DIL}(x, y) \right] \quad (6)$$

269 where

- 270 •  $L_{p,IEM}$  is the osmotic water permeability coefficient of a generic Ion Exchange
- 271 Membrane ( $IEM$ ), i.e. either the cation- or the anion-exchange membrane ( $CEM$  or
- 272  $AEM$ ), whose value is usually given in ml/(m<sup>2</sup> h bar) but is expressed here in SI units
- 273 m<sup>3</sup>/(m<sup>2</sup> s Pa).

274 •  $\pi_{IEM}^{SOL}(x, y)$  is the osmotic pressure evaluated at the concentration  $C_{IEM}^{SOL}(x, y)$  occurring  
 275 at the interface between the generic *IEM* membrane and the generic *SOL* solution  
 276 (solution side). For simplicity, osmotic pressures were calculated here by the van't Hoff  
 277 law  $\pi_{IEM}^{SOL} = 2RTC_{IEM}^{SOL}$ .

278 The second transport mechanism, i.e. electro-osmosis, refers to the migration of water  
 279 molecules coupled with the ions' transport. The electro-osmotic term can be expressed as:

$$280 \quad J_W^{E.OSM}(x, y) = n_h N_{SALT}^{TOT}(x, y) \frac{M_w}{\rho_w} \quad (7)$$

281 where  $n_h$  is the hydration number, here assumed to be equal to 7, while  $M_w$  and  $\rho_w$  are the  
 282 water molecular weight (in kg/mol) and density (in kg/m<sup>3</sup>).

283 In regard to the total salt flux  $N_{SALT}^{TOT}(x, y)$ , it accounts for the Coulombic, or migrative, flux  
 284  $N_{Coul}^{TOT}(x, y)$  and the diffusive  $N_{Diff}^{TOT}(x, y)$  flux:

$$285 \quad N_{SALT}^{TOT}(x, y) = N_{Coul}^{TOT}(x, y) - N_{Diff}^{TOT}(x, y) \quad (8)$$

286 It is worth noting that the ion diffusive flux occurs from the concentrate channel to the  
 287 dilute one. Therefore, in ED, it has to be subtracted from the Coulombic ion flux, which is  
 288 directed from the dilute solution to the concentrated one. The Coulombic flux represents the  
 289 main salt transport contribution and is proportional to the local ionic current density  $i_c$ . For  
 290 monovalent ions, under the assumption of unitary membrane perm-selectivity, the Na<sup>+</sup> ions flux  
 291  $N_{Coul}^{Na^+}(x, y)$  through a *CEM*, or the Cl<sup>-</sup> ions flux  $N_{Coul}^{Cl^-}(x, y)$  through an *AEM*, which correspond  
 292 to the total Coulombic flux, can be expressed by the Faraday law as:

$$293 \quad N_{Coul}^{Na^+ \text{ or } Cl^-}(x, y) = \frac{i_c(x, y)}{z_{Na^+ \text{ or } Cl^-} F} \quad (9)$$

294 where  $F$  is the Faraday constant (96,485 C/mol),  $i_c(x, y)$  is the local ionic current density in  
 295 A/m<sup>2</sup> and  $z_{Na^+ \text{ or } Cl^-}$  is the ion valence, i.e. +1 and -1 for Na<sup>+</sup> and Cl<sup>-</sup>, respectively.

296 As already discussed, the diffusive flux describes the salt back-diffusion through the  
 297 membrane due to the concentration difference between the channels. The diffusive flux through  
 298 a single membrane can be written as:

$$299 \quad N_{Diff}^{IEM}(x, y) = \frac{D^{IEM}}{t} [C_{IEM}^{CON}(x, y) - C_{IEM}^{DIL}(x, y)] \quad (10)$$

300 where  $D^{IEM}$  is the salt diffusivity in a generic *IEM* membrane of thickness  $t$ . Two diffusive  
 301 fluxes, one at the *AEM* and one at the *CEM*, have to be taken into account, so that  
 302  $N_{Diff}^{TOT}(x, y) = N_{Diff}^{AEM}(x, y) + N_{Diff}^{CEM}(x, y)$ .

303

## 304 **2.2 Electric variables, Ohmic and non-Ohmic resistances**

305 In ED systems, the overall voltage drop over a cell pair  $V_{cp}$ , independent of  $x$  and  $y$  as will  
 306 be discussed in Section 2.3, can be expressed as:

$$307 \quad V_{cp} = \eta(x, y) + R_{TOT}(x, y)i_c(x, y) \quad (11)$$

308 The term  $\eta(x, y)$  is the non-Ohmic voltage drop and  $R_{TOT}(x, y)i_c(x, y)$  is the Ohmic loss in  
 309 the cell pair.  $R_{TOT}$  is the total areal resistance of the cell pair and can be expressed as:

$$310 \quad R_{TOT}(x, y) = R^{CEM}(x, y) + R^{AEM}(x, y) + R^{DIL}(x, y) + R^{CON}(x, y) \quad (12)$$

311 where  $R^{CEM}(x, y)$  and  $R^{AEM}(x, y)$  are the areal electrical resistances of the membranes, while  
 312  $R^{DIL}(x, y)$  and  $R^{CON}(x, y)$  are the areal electrical resistances of the channels.

313 By following the results of the experimental measurements performed by Galama *et al.*  
 314 [51],  $R^{IEM}(x, y)$  can be approximated as:

$$315 \quad R^{IEM}(x, y) = a^{IEM} + b^{IEM} \left[ C_{IEM}^{DIL}(x, y) \right]^{-c^{IEM}} \quad (13)$$

316 where  $a^{IEM}$ ,  $b^{IEM}$ ,  $c^{IEM}$  are constants, which can be empirically determined. In the present  
 317 simulations,  $a$  was set equal to  $1.89 \times 10^{-4}$  and  $1.77 \times 10^{-4} \Omega \text{ m}^2$ , for the *CEM* and *AEM*  
 318 membranes, respectively. These values are the areal membrane resistances measured at the  
 319 standard concentration of 0.5M NaCl. Moreover,  $b$  and  $c$  are equal to  $7 \times 10^{-3}$  (in the appropriate  
 320 units) and 1.25, for both *AEM* and *CEM*. The constants were taken from [46].

321 In regard to the channel areal resistance, it can be estimated by:

$$322 \quad R^{SOL}(x, y) = \frac{h^{SOL}(x, y)}{\kappa^{SOL}(x, y)\varepsilon^2(x, y)} \quad (14)$$

323 where  $\kappa^{SOL}(x, y)$  is the electrical conductivity of the solution, which is a function of the local  
 324 salt concentration (as expressed by Eqs. (A.2-3)),  $\varepsilon(x, y)$  is the local channel volume porosity,  
 325 defined with reference to the unit cell as the ratio between fluid volume and total volume of the  
 326 undeformed channel without profiles, while  $h^{SOL}(x, y)$  is the local equivalent channel thickness,  
 327 defined as the ratio of fluid volume to projected area of a unit cell. The fluid volume ( $V_f$ ) under  
 328 deformed condition is a function of the local TMP [31]. In the present work, it is computed by

329 a polynomial approximation of results obtained for a variety of membrane profiles by the one-  
 330 way coupled fluid-structure simulations described in [29,30]. In particular, for the OCF profiled  
 331 membranes with  $P/H=8$  considered here, the dependence of  $V_f$ ,  $h^{SOL}$  and  $\varepsilon$  on TMP is reported  
 332 in Appendix B (Eqs. (B.2-4)).

333 Eq. (14) is, of course, only a crude approximation for the Ohmic resistance of the solution  
 334 flowing in its channel, based, in particular, on the assumption that membrane profiles do not  
 335 contribute significantly to the total conductance. In order to accurately investigate its validity,  
 336 its predictions were compared with accurate 3D numerical solutions of the Laplace equation for  
 337 the electrical potential [45]; only minor discrepancies were obtained, thanks also to the fact that  
 338 the OCF geometry investigated ( $P/H=8$ ) is characterized by a channel porosity close to 0.9, so  
 339 that the accurate modelling of the profiles is not a crucial issue.

340 In Eq. (11), both non-Ohmic voltage drop  $\eta(x, y)$  and Ohmic resistances were presented. With  
 341 regard to  $\eta(x, y)$ , it is given by the back electro-motive force originated from the salt  
 342 concentration gradient over the perm-selective membranes.  $\eta(x, y)$  can be divided into two  
 343 contributions associated with (i) the concentration gradient between the two solutions bulks  
 344  $\varphi(x, y)$  and (ii) its increment due to concentration polarization phenomena  $\eta_{BL}(x, y)$ .

345 Therefore, the total non-Ohmic voltage drop can be written as:

$$346 \quad \eta(x, y) = \varphi(x, y) + \eta_{BL}(x, y) \quad (15)$$

347 Specifically, the first contribution for a single membrane IEM is calculated [32] as:

$$348 \quad \varphi_{IEM}(x, y) = (\alpha_{IEM}) \frac{RT}{F} \ln \left( \frac{\gamma^{CON}(x, y) C_{Bulk}^{CON}(x, y)}{\gamma^{DIL}(x, y) C_{Bulk}^{DIL}(x, y)} \right) \quad (16)$$

349 where  $\alpha_{IEM}$  is the perm-selectivity of a generic membrane, which is correlated to the ability of  
 350 the membrane to block the passage of co-ion through itself (assumed constant in the model);  $T$   
 351 is the temperature;  $R$  is the gas constant;  $\gamma^{CON}$  and  $\gamma^{DIL}$  are the salt activity coefficients in the  
 352 *CON* and *DIL* solutions (calculated using Eqs. (A.6-7)), which depend on the solution bulk  
 353 concentration ( $C_{Bulk}^{CON}(x, y)$  and  $C_{Bulk}^{DIL}(x, y)$ ). Taking into account both *AEM* and *CEM*  
 354 membranes, one has:  $\varphi(x, y) = \varphi_{AEM}(x, y) + \varphi_{CEM}(x, y)$ .

355 The second contribution in Eq. (15) accounts for concentration polarization phenomena.  
 356 Concentration polarization phenomena are caused by the different kinetics of ion transport in  
 357 solutions and in membranes [2]. In particular, polarization phenomena can be defined as: “the  
 358 concentration profile that has a higher (or lower) level of solute nearest to the upstream  
 359 membrane surface compared with the more-or-less well-mixed bulk fluid far from the

360 membrane surface” [52]. In the case of the ED process, salt concentration increases at the  
 361 membrane surface in the concentrate channel and reduces at the membrane surface in the diluate  
 362 channel causing a non-Ohmic voltage drop, which is opposite to the external applied voltage,  
 363 thus reducing process’ performance.

364 Non-Ohmic voltage drop due to concentration polarization can be calculated at each  
 365 solution-membrane interface of a cell pair, therefore the total contribution is represented by the  
 366 sum of four boundary layers:

$$367 \quad \eta_{BL}(x, y) = \eta_{AEM}^{CON}(x, y) + \eta_{CEM}^{CON}(x, y) + \eta_{AEM}^{DIL}(x, y) + \eta_{CEM}^{DIL}(x, y) \quad (17)$$

368 where the voltage drop  $\eta_{IEM}^{SOL}(x, y)$  at the generic *IEM* membrane, i.e. *AEM* or *CEM*, in contact  
 369 with the generic solution *SOL* (*CON* or *DIL*), can be calculated as [45]:

$$370 \quad \eta_{IEM}^{SOL}(x, y) = -\alpha_{IEM} \frac{RT}{F} \ln(\theta_{IEM}^{SOL}(x, y)) \quad (18)$$

371 where  $\theta_{IEM}^{SOL}(x, y)$  is the so-called polarization coefficient determined at the membrane-solution  
 372 interface as:

$$373 \quad \theta_{IEM}^{CON}(x, y) = \frac{C_{Bulk}^{CON}(x, y)}{C_{IEM}^{CON}(x, y)} \quad \text{and} \quad \theta_{IEM}^{DIL}(x, y) = \frac{C_{IEM}^{DIL}(x, y)}{C_{Bulk}^{DIL}(x, y)} \quad (19)$$

374 Note that,  $\theta_{IEM}^{CON}(x, y)$  and  $\theta_{IEM}^{DIL}(x, y)$  are always smaller than one. In Eq. (19), the effects of the  
 375 activity coefficients are neglected.

376 To determine the polarization coefficients in Eq. (19), information about  $C_{IEM}^{CON}(x, y)$  and  
 377  $C_{IEM}^{DIL}(x, y)$  is needed. To this aim, the *Sherwood* number equation presented in [45] is employed:

$$378 \quad Sh_{IEM}^{SOL}(x, y) = \left| \frac{(N_{Diff}^{IEM}(x, y) + 0.5 \times N_{Coul}^{TOT}(x, y)) 2H}{(C_{Bulk}^{SOL}(x, y) - C_{IEM}^{SOL}(x, y)) D^{SOL}(x, y)} \right| \quad (20)$$

379 where  $D^{SOL}(x, y)$  is the salt diffusivity in the generic solution *SOL*, whose dependence on the  
 380 solution concentration is expressed in Eqs. (A.4-5). The term  $N_{Diff}^{IEM}(x, y) + 0.5 \times N_{Coul}^{TOT}(x, y)$   
 381 represents the diffusive salt flux in the generic solution *SOL* in contact with the generic  
 382 membrane *IEM*, which can be found by taking into account the flux continuity at the solution-  
 383 membrane interface.

384 Rearranging Eq. (20) and taking into account Eq. (19), the polarization coefficients for the  
 385 two solutions can be calculated as:

$$386 \quad \theta_{IEM}^{CON}(x, y) = 1 / \left[ 1 + \frac{(N_{Diff}^{IEM}(x, y) + 0.5 \times N_{Coul}^{TOT}(x, y)) 2H}{Sh_{IEM}^{CON}(x, y) C_{Bulk}^{CON}(x, y) D_{Salt}^{CON}(x, y)} \right] \quad (21)$$

387 
$$\theta_{IEM}^{DIL}(x, y) = 1 - \frac{(N_{Diff}^{IEM}(x, y) + 0.5 \times N_{Coul}^{TOT}(x, y))2H}{Sh_{IEM}^{DIL}(x, y)C_{Bulk}^{DIL}(x, y)D_{Salt}^{DIL}(x, y)} \quad (22)$$

388 Thus, the voltage drop  $\eta_{IEM}^{SOL}(x, y)$  can be obtained from Eq. (18).

389

### 390 **2.3 Stack description**

391 In the ED system, a potential voltage drop  $V$  is applied by a power supply to the electrodes  
 392 in order to obtain the desired desalination degree of the dilute ( $DIL$ ) feed solution. In the model,  
 393 the potential voltage drop  $V$  is assumed to be constant (i.e. independent of  $x$  and  $y$ ) at the  
 394 electrodes. At the stack level, the number of cell pairs and the electrode compartments have to  
 395 be taken into account in order to simulate the whole electrical circuit.

396 The local current density  $i_c(x, y)$  can be expressed as (Kirchhoff's second law):

397 
$$i_c(x, y) = \frac{V - \eta(x, y)N_{cp}}{R_{blank} + R_{TOT}(x, y)N_{cp}} \quad (23)$$

398 where  $N_{cp}$  is the total number of cell pairs and  $R_{blank}$  is the electric resistance of the electrode  
 399 compartments.

400 The total power consumption of the process  $P_{el}$  can be expressed as:

401 
$$P_{el} = VI + P_{pump} \quad (24)$$

402 where  $I$  is the overall current calculated as the integral of the current density ( $i_c$ ) over the active  
 403 area of the membrane, while  $P_{pump}$  is the total pumping power. This latter quantity is quite  
 404 cumbersome to compute in the presence of trans-membrane fluxes (due to osmotic and electro-  
 405 osmotic effects) which make the flow rate of either solution differ from inlet to outlet, especially  
 406 in the present, two-dimensional domain. A crude approximation is

407 
$$P_{pump} = \frac{\Delta p^{CON} Q_{TOT,av}^{CON}}{\eta_{pump}^{CON}} + \frac{\Delta p^{DIL} Q_{TOT,av}^{DIL}}{\eta_{pump}^{DIL}} \quad (25)$$

408 in which  $\Delta p^{SOL}$  is the inlet-to-outlet distributed pressure drop associated with either solution  
 409 (singular losses in the manifolds and in the piping are not included in the present model), while  
 410  $Q_{TOT,av}^{SOL}$  is the flow rate in either channel, averaged between inlet and outlet and summed up over  
 411 the  $N_{cp}$  cell pairs (assumed identical in the present model).

412 Finally, two other important parameters can be introduced to quantify the efficiency of an  
 413 ED stack [46]:

- 414 • The energy consumption per unit volume of product  $E_{spec}$  :

415 
$$E_{spec} = \frac{P_{el}}{Q_{TOT,OUTLET}^{DIL}} \quad (26)$$

416 where  $Q_{TOT,OUTLET}^{DIL}$  is the overall diluate outlet flowrate from all cell pairs.

- 417 • The apparent product flux  $J_p$  :

418 
$$J_p = \frac{Q_{TOT,OUTLET}^{DIL}}{2LWN_{cp}} \quad (27)$$

419 which can be useful in order to calculate the total membrane area required to obtain a certain  
420 flow rate of desalinated water.

421 For the sake of clarity, Table 1 summarizes all the constants employed for membrane and  
422 channels features. The correlations used for the physical and transport properties of NaCl  
423 solutions are reported in Appendix A.

424

425 **Table 1.** Values of the fixed quantities employed in the model. Many of these parameters were taken  
426 from [53].

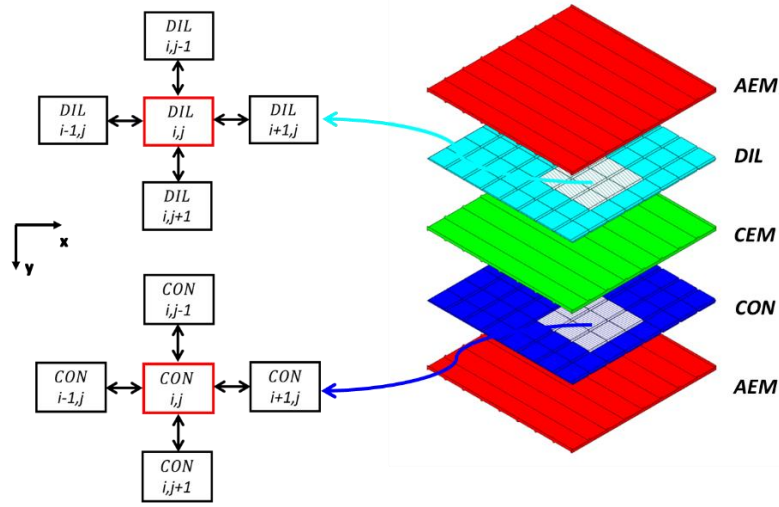
Quantity	Value	Unit
Temperature	25	°C
Nominal channel height $H$ ( <i>DIL</i> and <i>CON</i> )	$200 \times 10^{-6}$ [29,31]	m
Undeformed channel porosity $\varepsilon$ ( <i>DIL</i> and <i>CON</i> )	0.9 [29,31]	-
Membrane thickness ( <i>AEM</i> and <i>CEM</i> )	$120 \times 10^{-6}$ [29,31]	m
Salt diffusivity, $D_{Salt}^{IEM}$ ( <i>AEM</i> and <i>CEM</i> )	$4e^{-12}$ [53]	m <sup>2</sup> /s
<i>AEM</i> permselectivity, $\alpha_{AEM}$ (constant)	0.969 [53]	-
<i>CEM</i> permselectivity, $\alpha_{CEM}$ (constant)	0.975 [53]	-
Water permeability in the <i>AEM</i> , $L_{p,AEM}$	6.29 [53]	ml/m <sup>2</sup> h bar
Water permeability in the <i>CEM</i> , $L_{p,CEM}$	7.79 [53]	ml/m <sup>2</sup> h bar
Blank resistance, $R_{blank}$	$2 \times 10^{-3}$ [53]	$\Omega$ m <sup>2</sup>

427

## 428 2.4 Resolution algorithm

429 In order to solve the water and salt mass balance equations (1)-(4) taking account of the  
430 constitutive equations (5-23) described in the previous Section, a finite difference approach,  
431 similar to that used in [31], is adopted. The two *CON* and *DIL* channels of a cell pair, of overall  
432 size  $L \times W$ , are divided into a number of rectangular blocks along the  $x$  ( $N_{Block}^x$ ) and  $y$  ( $N_{Block}^y$ )  
433 directions, of size  $\Delta x = L / N_{Block}^x$  and  $\Delta y = W / N_{Block}^y$ . Figure 4 presents a sketch of a cell pair

434 along with a detail of the computational molecules adopted in the present work to compute  
 435 spatial derivatives in Eqs. (1-4).



436

437 **Figure 4.** Schematic representation of a cell pair made of a diluate channel (*DIL*), a concentrate channel  
 438 (*CON*), an *AEM* and a *CEM* (a further *AEM* membrane is added only to illustrate the periodicity of the  
 439 cell pair). In addition, details of the computational molecules adopted for the discretization of Eqs. (1-  
 440 4) in both channels are reported on the right. Adapted from [31].

441 With reference to the computational molecules shown in Figure 4, multiplying all terms in  
 442 Eqs. (1)-(4) by the nominal volume of a block,  $H\Delta x\Delta y$ , approximating the derivatives by finite  
 443 differences, and neglecting in each channel the components of the velocity along the direction  
 444 orthogonal to the main flow, with reference to the flow configuration of Figure 3, the following  
 445 salt / water discrete mass balance equations are obtained:

446 
$$C_{Bulk;i,j}^{CON} \cdot Q_{i,j}^{CON;x} - C_{Bulk;i-1,j}^{CON} \cdot Q_{i-1,j}^{CON;x} = N_{SALT;i,j}^{TOT} \cdot \Delta x\Delta y \quad (28)$$

447 
$$Q_{i,j}^{CON;x} - Q_{i-1,j}^{CON;x} = J_{W;i,j}^{TOT} \cdot \Delta x\Delta y \quad (29)$$

448 
$$C_{Bulk;i,j}^{DIL} \cdot Q_{i,j}^{DIL;y} - C_{Bulk;i,j-1}^{DIL} \cdot Q_{i,j-1}^{DIL;y} = -N_{SALT;i,j}^{TOT} \cdot \Delta x\Delta y \quad (30)$$

449 
$$Q_{i,j}^{DIL;y} - Q_{i,j-1}^{DIL;y} = -J_{W;i,j}^{TOT} \cdot \Delta x\Delta y \quad (31)$$

450 where  $Q_{i,j}^{CON;x}$  is the flow rate in the *CON* channel, directed along  $x$  from block  $(i, j)$  to block  
 451  $(i+1, j)$  while  $Q_{i,j}^{DIL;y}$  is the flow rate in the *DIL* channel, directed along  $y$  from block  $(i, j)$  to  
 452 block  $(i, j+1)$ .  $J_{W;i,j}^{TOT}$  is the specific trans-membrane water flux (in m/s) from the diluate to the  
 453 concentrate channel in block  $(i,j)$ .  $N_{SALT;i,j}^{TOT}$  is the specific trans-membrane salt flux, in  
 454 mol/(m<sup>2</sup>s), from the diluate to the concentrate channel in block  $(i,j)$ . Finally,  $C_{Bulk;i,j}^{SOL}$  is the bulk  
 455 salt concentration, in mol/m<sup>3</sup>, in the generic *SOL* channel (either *CON* or *DIL*) in block  $(i,j)$ .

456 The fluid flow may have a nonzero component in the direction orthogonal to the main flow.  
457 However, our previous investigation on cross-flow configurations with uniform conditions at  
458 the inlet (velocity) and at the outlet (pressure) [31] revealed that such secondary velocity  
459 components are still three orders of magnitude lower than the streamwise component even in  
460 the presence of relevant TMP values (see Figure 12(f) in [31]). This consideration justifies the  
461 assumption made here.

462 Eqs. (28-31) are  $4N$  equations in  $4N$  unknowns, where  $N = N_{Block}^x \cdot N_{Block}^y$  :  $N$  concentrations  
463 in the *CON* channel,  $N$  concentrations in the *DIL* channel,  $N$  flow rates along  $x$  in the *CON*  
464 channel and  $N$  flow rates along  $y$  in the *DIL* channel.

465 All the terms in the constitutive Eqs. (5-23) are evaluated at each grid block taking into  
466 account the local concentration of the two solutions.

467 In order to couple Eqs. (28-31) and (5-23), thus determining the steady-state distributions  
468 of all variables for a chosen ED stack configuration, an iterative procedure is employed. In  
469 particular, the algorithm can be divided into four main steps:

470

471 I. Starting from a tentative pressure distribution in the two channels, the local TMP is  
472 evaluated in each block. The local hydraulic permeability  $K$  resulting from the TMP-induced  
473 deformation is then calculated by using  $K$ -TMP correlations, Eq. (B.1) in Appendix B, derived  
474 from previous local-scale studies of the fluid-structure interaction for the same OCF geometry  
475 [29]. The simplified (Darcyan) model described in Section 2.4 of ref. [31] is then used to  
476 compute the flow rates  $Q$ . At this stage, trans-membrane water fluxes are neglected.

477

478 II. All the other distributed variables are then computed by the ED process model solving  
479 Eqs. (5-23) in conjunction with the salt balance equations (28) and (30) for the chosen value of  
480 the applied voltage and of the number of cell pairs.

481 Step II is iterated until a desired convergence criterion is satisfied. More specifically, at the  
482 beginning of step II uniform block concentrations, equal to the inlet values ( $C_{Inlet}^{DIL}, C_{Inlet}^{CON}$ ), are  
483 imposed in both channels at each grid block, and the same values are also assumed for the  
484 membrane-solution interfacial concentrations (no concentration polarization).

485 Then, the solution's properties and activity coefficients are calculated by the correlations  
486 reported in Appendix A Eqs. (A1-7). The channels' Ohmic resistances are evaluated by Eq.  
487 (14), taking into account the channel equivalent height and local porosity, which are computed  
488 from the TMP distribution obtained in step I using Eqs. (B.3) and (B.4) in Appendix B.  
489 Membrane resistances are calculated by Eq. (13) and thus the cell pair resistance can be

490 obtained by Eq. (12). The non-Ohmic voltage drop  $\varphi$  and  $\eta$  are evaluated by Eqs. (16) and  
491 (15) at each grid block. Note that the voltage drop due to concentration boundary layers  $\eta_{BL}$   
492 and also  $\varphi$  are zero at the first iteration, since bulk and interfacial concentrations are the same.  
493 The local current density  $i_c$  is obtained from Eq. (23).

494 By knowing the current density and solution concentrations, total salt and water fluxes are  
495 calculated using Eqs. (5-10). Thus, polarization coefficients and  $\eta_{BL}$  can be found by Eqs. (17,  
496 18, 21, 22) by using Eqs. (B.5-18) to calculate Sherwood numbers as functions of local TMP.  
497 Note that  $\eta_{BL}$  is actually used at the next iteration to compute  $\eta$ .

498 Finally, from Eqs. (28) and (30) new concentration values at each  $i, j$  block are found. Step  
499 II terminates when the maximum difference between old and new concentrations over all grid  
500 blocks ( $e = |C_{New}^{SOL} - C_{Old}^{SOL}|$ ) becomes less than  $10^{-3}$  M.

501

502 III. Flow rates of step I are re-calculated using the water balance equations (29) and (31)  
503 taking into account the trans-membrane water fluxes calculated in step II.

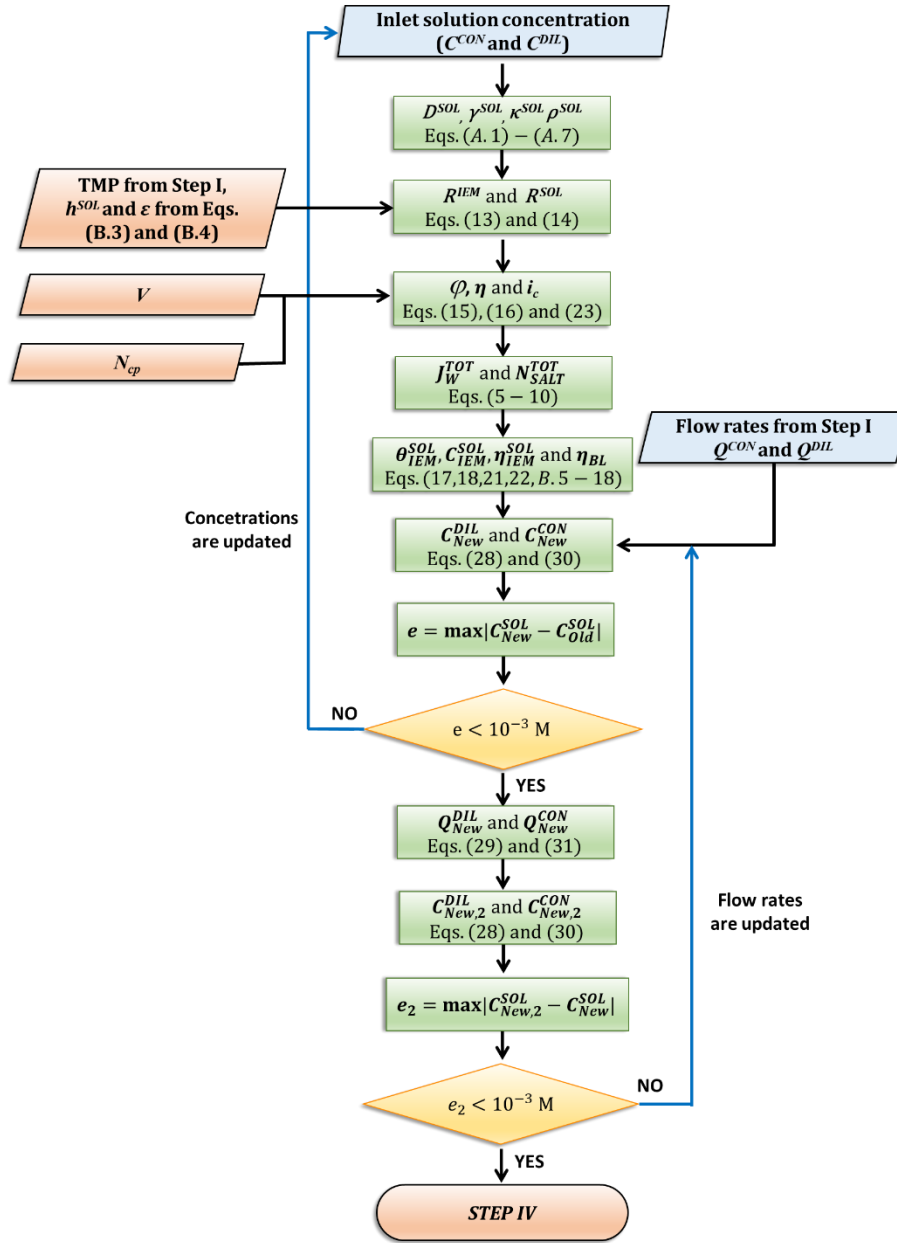
504 Then, the solution concentrations ( $C_{New,2}^{SOL}$ ) are again calculated from the mass balances of  
505 Eqs. (28) and (30), taking into account the new flow distribution. Finally, the difference  
506 between the new concentration values and those of step II are calculated over all grid blocks as  
507  $e_2 = |C_{New,2}^{SOL} - C_{New}^{SOL}|$ . If the maximum difference is higher than  $10^{-3}$  M, the flow distribution is  
508 updated in step II and new concentrations are found. Otherwise, the final solution is attained.  
509 For the sake of clarity, Figure 5 presents the flow chart of Steps II and III.

510

511 IV. Finally, the process' performances are evaluated by solving Eqs. (24-27).

512 It should be noted that, in a more complete procedure, membrane deformation (deformed  
513 membrane shape) would be updated (step I) considering the calculated flow rates of step III,  
514 which take into account water transmembrane fluxes. However, this step has been neglected in  
515 the present version of the model in view of the small influence of the trans-membrane water  
516 flow rate with respect to the main water flow rate along the channels. A more detailed discussion  
517 of this issue was presented in [31].

518 The procedure was implemented in the Matlab environment.



519

520 **Figure 5.** Flow chart of steps II and III of the iterative algorithm used for the 2-D process model of ED  
521 stacks.

522

## 523 2.5 Grid dependence analysis

524 In order to determine the most suitable grid size that satisfies the trade-off between  
525 computing time and accuracy in the simulation of cross-flow configurations, a sensitivity  
526 analysis of the model predictions on the grid resolution was carried out. In this grid dependence  
527 analysis, membrane deformation effects were taken into account. Five grids were investigated:  
528 40×40, 80×80, 120×120, 180×180 and 240×240 blocks. All simulations were conducted for ED  
529 stacks equipped with OCF profiled membranes with  $P/H=8$ , see Figure 2, assuming:

530

- inlet solutions concentrations of 513.34 mol/m<sup>3</sup> (30 g/l);

531

- length and width of the stack equal to 0.6 m;

- 532 • inlet mean concentrate and diluate velocities of 5 cm/s;
- 533 • 400 cell pairs;
- 534 • an applied voltage drop  $V$  able to desalinate the diluate up to an outlet concentration of
- 535  $8.5 \text{ mol/m}^3$  (0.5 g/l).

536 Moreover, the parameters in Table 1 were used. Table 2 and Figure 6 present the results of  
 537 the above mentioned grid-dependence analysis. Reported discrepancies are with respect to the  
 538 finest grid (240×240).

539

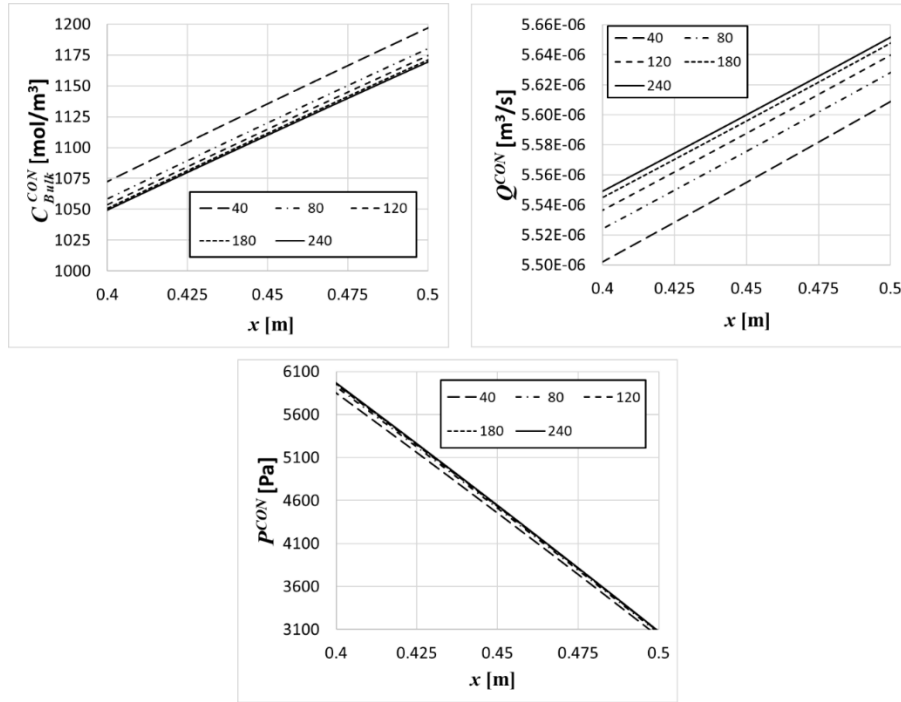
540

**Table 2.** Grid dependence for the cross-flow configuration.

$N_{Block}^x = N_{Block}^y$	40	80	120	180	240
<b>Quantities</b>					
$C_{OUTLET}^{CON}$ [M]	969.41	966.59	965.76	965.21	964.93
<b>Discrepancy %</b>	0.464	0.172	0.086	0.029	0.000
$Q_{TOT,OUTLET}^{CON}$ [l min <sup>-1</sup> ]	151.16	152.52	152.96	153.27	153.43
<b>Discrepancy %</b>	-1.480	-0.593	-0.306	-0.104	0.000
$Q_{TOT,OUTLET}^{DIL}$ [l min <sup>-1</sup> ]	130.11	131.67	132.16	132.51	132.69
<b>Discrepancy %</b>	-1.944	-0.769	-0.399	-0.136	0.000
$V$ [V]	260.15	254.99	253.70	252.90	252.50
<b>Discrepancy %</b>	3.030	0.986	0.475	0.158	0.000
$i_c$ [A m <sup>-2</sup> ]	839.75	831.52	828.73	827.19	826.43
<b>Discrepancy %</b>	1.612	0.616	0.278	0.092	0.000

541

542 Note that  $C_{OUTLET}^{CON}$  is calculated as the mean concentration value at the outlet of the  
 543 concentrate channel;  $Q_{TOT,OUTLET}^{CON}$  is the overall concentrate outlet flowrate, calculated as the flow  
 544 rate at the outlet of the channel and multiplied by the total number of cell pairs ( $N_{cp}$ ).



545

546 **Figure 6.** Comparison among results of the present model obtained with different discretization degrees:  
 547 concentration, flow rate and pressure profiles of the concentrate solution along a line placed at 2.5 cm  
 548 from the top of the channel. Quantities in the region of the channel between 0.4 and 0.5 m are reported.

549

550 Results show that the 80×80 grid can be employed, as discrepancies lower than 1% are  
 551 obtained with respect to the finest grid. Note that all the results shown hereinafter are obtained  
 552 using the 80×80 grid.

553

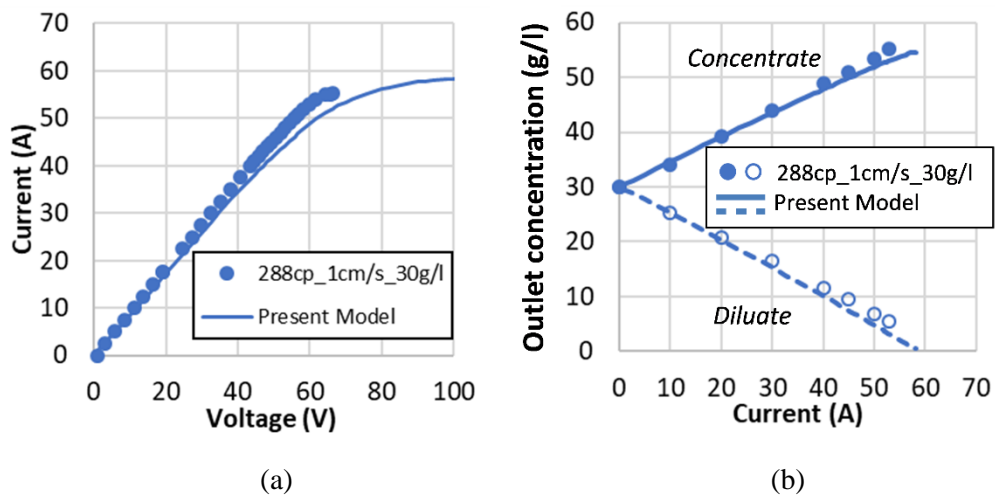
## 554 2.6 Model validation

555 The electrochemical part of the model was validated by comparison with experimental  
 556 results provided by the REDstack company for an ED square cross-flow stack of 0.44 m side  
 557 with 288 cell pairs. The stack was equipped with woven spacers having  $P/H=2$ , a porosity of  
 558 0.712 and a nominal channel height  $H$  of 260  $\mu\text{m}$ . Fujifilm Type 10 Ion Exchange Membranes  
 559 (FujiFilm Manufacturing Europe B.V.), which are the same membranes described in this work,  
 560 were used. Both salt solutions were fed at a superficial velocity ( $U^{SOL}$ ) of 1 cm/s and at an  
 561 initial solution concentration of 513.34 mol/m<sup>3</sup> (30 g/l). The applied voltage  $V$  was made to vary  
 562 between 0 and ~65 V. The temperature was measured to increase from 18 to 22°C during the  
 563 experiments due to the passage of electric current, and these changes (which affect solution and  
 564 membrane properties and also the electromotive force) were explicitly included in the  
 565 simulations. The empirical correlations for the solution and the membrane resistances are  
 566 reported in the Appendix A. The voltage data provided do not take electrode losses into account,

567 thus null blank resistance ( $R_{blank}$ ) was set in the simulation. In order to account for the different  
 568 spacer configuration with respect to the OCF profiled membranes discussed so far, the  
 569 Sherwood number and friction factor dependence on the fluid velocity appropriate to channels  
 570 filled with woven spacers, as obtained in [45], were implemented in the model.

571 The test conditions (woven spacers of small  $P/H$ , moderate flow velocities) are such that  
 572 no significant membrane/channel deformation is expected to have occurred. Therefore, no  
 573 membrane deformation was taken into account in the simulations. Comparison between the  
 574 experimental and the numerical current-voltage and outlet concentration-current curves are  
 575 shown in Figure 7.

576



577

578

579 **Figure 7.** Experimental results (symbols) and predictions by the present model (lines) for an ED cross-  
 580 flow stack. (a) current-voltage curves; (b) outlet concentration-current curves. In graph (b), solid lines  
 581 and symbols represent the concentrate outlet concentration, while dashed lines and hollow symbols  
 582 represent the diluate outlet concentrations.

583

584 From Figure 7, it can be observed that the model predictions are in very good agreement  
 585 with the experiments, both in terms of electric variables and of outlet concentrations, though  
 586 approaching limiting current conditions generates a slight deviation of model results from  
 587 experimental data.

588

### 589 3 Model results

#### 590 3.1 No membrane deformation

591 To investigate the process performances of cross-flow ED stacks for seawater desalination  
 592 (inlet solutions concentrations of  $513.34 \text{ mol/m}^3$ , i.e. 30 g/l) depending on the size and the  
 593 operating conditions, a first parametrical study was carried out neglecting deformation effects.

594 As discussed in Section 2, limiting current density conditions are not well reproduced by the  
 595 model. Therefore, in order to avoid simulating working conditions where limiting current  
 596 density may arise, it was decided to simulate two consecutive ED stacks in series with the same  
 597 features, except the inlet solutions concentrations. Specifically, the first stack was fed by salt  
 598 solutions of initial concentration of  $513.34 \text{ mol/m}^3$  (30 g/l). In this stack, a first desalination  
 599 step took place reducing the concentration of one of the two streams to  $85.5 \text{ mol/m}^3$  (5 g/l). The  
 600 outlet solutions were then directly pumped into the second stack, which completed the  
 601 desalination process by reducing the diluate solution concentration to  $8.55 \text{ mol/m}^3$  (0.5 g/l). The  
 602 number of cell pairs was fixed at 400 for each case and each stack. All results were obtained  
 603 for OCF profiled membranes with  $P/H=8$ , see Figure 2, having an equivalent undeformed  
 604 channel height  $h^{SO_L}$  of  $180 \mu\text{m}$ .

605 As far as the parametrical study is concerned, the length ( $L$ ) and the width ( $W$ ) of the stacks  
 606 were made to vary between 0.1 and 0.6 m. Moreover, the inlet velocity of the concentrate,  $v_c$ ,  
 607 and dilute,  $v_d$ , solutions in the first stack were made to vary between 1 and 5 cm/s. The total  
 608 voltage drop  $V$  at the electrodes of each stack yielding an outlet diluate concentration of  $85.5$   
 609  $\text{mol/m}^3$  for the first stack and  $8.55 \text{ mol/m}^3$  for the second stack was assessed in each simulated  
 610 case. All other quantities were kept fixed at the values listed in Table 1. Eight different cases  
 611 were investigated, as listed in Table 3.

612  
 613

**Table 3.** Eight ED stack configurations investigated in 2-stage desalination.

<i>Cases</i>	#1	#2	#3	#4	#5	#6	#7	#8
<i>Quantities</i>								
$L$ [m]	0.2	0.4	0.6	0.6	0.6	0.6	0.6	0.6
$W$ [m]	0.6	0.6	0.6	0.35	0.15	0.6	0.6	0.6
$v_c$ [cm/s]	5	5	5	5	5	3	1	1
$v_d$ [cm/s]	1	1	1	1	1	1	1	3

614

615 Results in terms of specific energy consumption  $E_{spec}$ , apparent flux  $J_p$ , overall electric  
 616 current of the first  $I^1$  and second  $I^2$  stack, voltage drop at the first  $V^1$  and second  $V^2$  stack,  
 617 diluate Ohmic resistance of the first  $R_{DIL}^1$  and second  $R_{DIL}^2$  stack and diluate flow rate at the outlet  
 618 of the second stack,  $Q_{TOT,OUTLET}^{DIL,2}$ , are reported in

619 Table 4. Ohmic resistances of the *CON* channels are not reported since they are small and  
 620 play a minor role in the overall voltage drop.

621 It should be noted that Eqs. (26) and (27) were modified as follows to address the  
 622 performances of the two consecutives stacks.

- 623 • Specific energy consumption:

$$624 \quad E_{spec}^{TOT} = \frac{P_{el}^1 + P_{el}^2}{Q_{TOT,OUTLET}^{DIL,2}} \quad (32)$$

625 where  $P_{el}^1$  and  $P_{el}^2$  are the electric power of the first and second stack, respectively, while  
 626  $Q_{TOT,OUTLET}^{DIL,2}$  refers to the overall diluate outlet flowrate of the second stack.

- 627 • Apparent product flux  $J_p^{TOT}$ :

$$628 \quad J_p^{TOT} = \frac{Q_{TOT,OUTLET}^{DIL,2}}{A^{TOT}} \quad (33)$$

629 where  $A^{TOT}$  is the total membrane area calculated as  $A^{TOT} = N_{Stacks} 2N_{cp} LW$ , where  $N_{stacks}$  is the  
 630 total number of stacks used in the desalination process, i.e. 2.

631

632 **Table 4.** Main results obtained for eight cross-flow 2-stage test cases in the absence of deformation.

<i>Cases</i>	<b>#1</b>	<b>#2</b>	<b>#3</b>	<b>#4</b>	<b>#5</b>	<b>#6</b>	<b>#7</b>	<b>#8</b>
<i>Quantities</i>								
$L$ [m]	0.2	0.4	0.6	0.6	0.6	0.6	0.6	0.6
$W$ [m]	0.6	0.6	0.6	0.35	0.15	0.6	0.6	0.6
$v_c$ [cm/s]	5	5	5	5	5	3	1	1
$v_d$ [cm/s]	1	1	1	1	1	1	1	3
$E_{spec}^{TOT}$ [kWh/m <sup>3</sup> ]	2.27	2.30	2.33	3.03	5.67	2.39	2.66	5.03
$J_p^{TOT}$ [l/m <sup>2</sup> h]	2.66	2.66	2.65	4.64	11.0	2.63	2.57	8.01
$I^1$ [A]	17.8	35.7	53.5	53.0	52.7	53.6	53.9	160
$I^2$ [A]	3.45	7.03	10.6	9.92	9.41	10.7	11.2	30.2
$V^1$ [V]	48.7	49.1	49.4	71.8	148	50.1	52.8	121
$V^2$ [V]	83.9	84.9	85.9	92.3	128	88.1	96.6	130
$R_{DIL}^1$ [ $\Omega$ ]	0.114	0.114	0.113	0.106	0.102	0.113	0.112	0.103
$R_{DIL}^2$ [ $\Omega$ ]	1.455	1.447	1.440	1.174	0.944	1.450	1.482	1.042
$Q_{TOT,OUTLET}^{DIL,2}$ [l min <sup>-1</sup> ]	8.52	17.0	25.4	26.0	26.4	25.3	24.7	76.9

633

634 Results suggest that the stack length ( $L$ , which is the length of the concentrate channel and  
635 the width of the diluate channel) does not significantly affect the process performances  
636 ( $E_{spec}^{TOT}$  and  $J_p^{TOT}$ ). In fact,  $E_{spec}^{TOT}$  and  $J_p^{TOT}$  are almost the same for cases #1-3.

637 The stack width ( $W$ , which is the width of the concentrate channel and the length of the  
638 diluate channel) considerably influences the process parameters, see results of cases #3, 4 and  
639 5. Specifically,  $E_{spec}^{TOT}$  and  $J_p^{TOT}$  are found to increase as the stack width  $W$  decreases. This can  
640 be explained considering that the stack width decreases from case #3 to case #5, while the  
641 diluate flow rate is almost constant at each case. This yields a reduction of the residence time  
642 of the dilute solution in the stack, which, in turn, causes an increase of the external potential to  
643 guarantee the same diluate outlet target concentration.

644 The specific energy consumption and the apparent flux change slightly when the  
645 concentrate solution velocity  $v_c$  varies, see cases #3 and 6-7. Conversely,  $E_{spec}^{TOT}$  and  $J_p^{TOT}$  are  
646 significantly affected by the diluate velocity  $v_d$  (cases #7-8). The effects of  $v_d$  exhibit an  
647 opposite trend with respect to that of the stack width  $W$ . Specifically, an increase of the diluate  
648 velocity causes an increase of both  $E_{spec}^{TOT}$  and  $J_p^{TOT}$ . This trend can be attributed to the change  
649 of the diluate solution residence time, as discussed for the influence of  $W$ .

650 It should be also noted that the comparison of cases #3 through 5, differing only in the stack  
651 width, illustrates the potential economic usefulness of a parametrical study such as the one  
652 conducted here. Although the reduction of the stack width yields an increase of the specific  
653 energy consumption, the desalination process requires less membrane area while demanding  
654 less concentrate flow rate and providing comparable outlet diluate flow rates (higher water  
655 recovery). This aspect may be taken into account in an economic optimization analysis, where  
656 the most convenient stack configuration is sought.

657

## 658 **3.2 Effects of membrane deformation**

659 The eight ED test cases presented above were also simulated taking into account membrane  
660 deformation effects. In particular, two membrane deformation conditions were investigated: (i)  
661 mild deformation and (ii) heavy deformation.

662

### 663 *3.2.1 Mild deformation effects*

664 To take membrane deformation into account, stationary flow and channel height  
665 distributions were first evaluated for each of the above mentioned eight cross-flow 2-stage cases

666 by computing step I of section 2.4 before performing steps II and III. As anticipated in Section  
667 2.4, quantities like the local hydraulic permeability  $K$ , the porosity  $\varepsilon$  and the equivalent channel  
668 height  $h^{SOL}$  resulting from the TMP-induced deformation were obtained by using correlations  
669 derived from previous local-scale studies of the fluid-structure interaction for the same  
670 membrane/channel geometry [29].

671 Table 5 reports the same quantities of Table 4 determined for all the eight cases taking  
672 deformation into account. In addition, the computed mean equivalent channel heights of the  
673 diluate channel for both stacks  $\langle h_{DIL}^1 \rangle$ ,  $\langle h_{DIL}^2 \rangle$  are also reported.

674

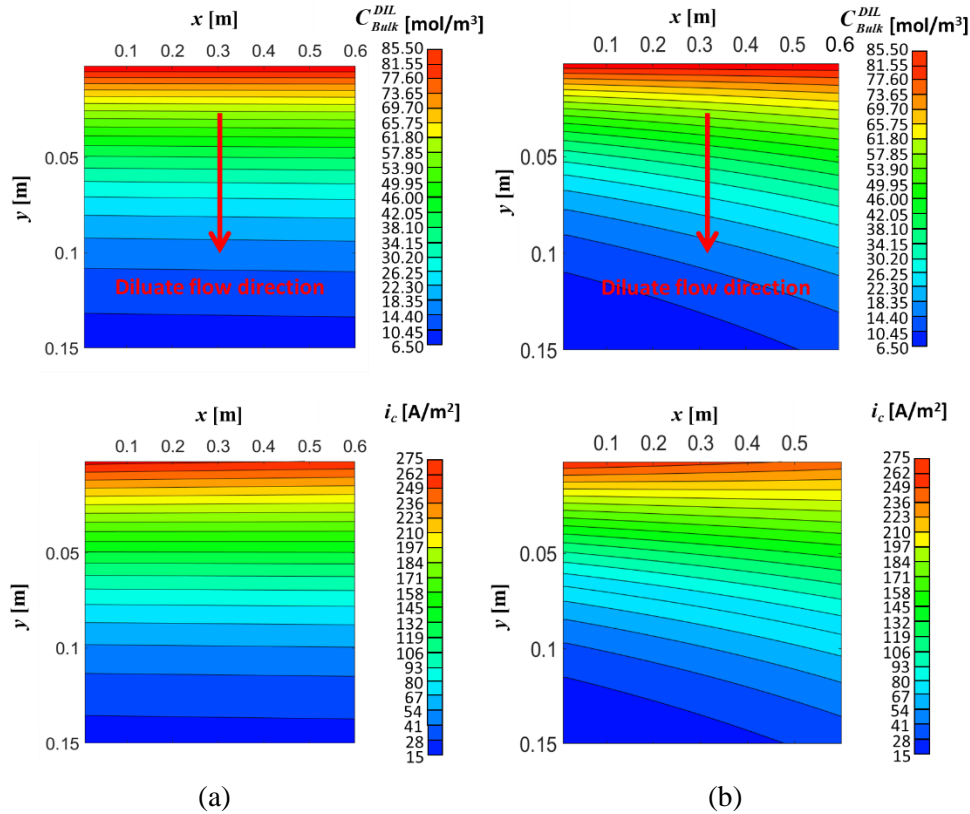
675 **Table 5.** Main results obtained for eight cross-flow test cases in the presence of deformation.

<i>Cases</i>	#1	#2	#3	#4	#5	#6	#7	#8
<i>Quantities</i>								
$L$ [m]	0.2	0.4	0.6	0.6	0.6	0.6	0.6	0.6
$W$ [m]	0.6	0.6	0.6	0.35	0.15	0.6	0.6	0.6
$v_c$ [cm/s]	5	5	5	5	5	3	1	1
$v_d$ [cm/s]	1	1	1	1	1	1	1	3
$E_{spec}^{Tot}$ [kWh/m <sup>3</sup> ]	2.26	2.28	2.31	2.99	5.53	2.37	2.64	4.98
$J_p^{Tot}$ [l/m <sup>2</sup> h]	2.68	2.66	2.69	4.65	11.2	2.66	2.60	8.10
$I^1$ [A]	17.9	35.6	53.7	52.9	52.7	53.7	54.1	160
$I^2$ [A]	3.52	7.04	10.7	9.92	9.52	10.8	11.3	30.5
$V^1$ [V]	48.7	48.8	49.3	71.2	146	50.0	52.7	120
$V^2$ [V]	83.4	84.4	85.5	91.3	124	87.7	96.2	129
$R_{DIL}^1$ [ $\Omega$ ]	0.113	0.112	0.111	0.105	0.100	0.112	0.113	0.105
$R_{DIL}^2$ [ $\Omega$ ]	1.44	1.42	1.40	1.14	0.92	1.43	1.48	1.04
$Q_{TOT,OUTLET}^{DIL,2}$ [l min <sup>-1</sup> ]	8.58	17.0	25.8	26.0	26.8	25.5	24.9	77.7
$\langle h_{DIL}^1 \rangle$ [ $\mu\text{m}$ ]	179	176	180	173	173	177	180	184
$\langle h_{DIL}^2 \rangle$ [ $\mu\text{m}$ ]	179	176	173	173	172	177	180	183

676

677 The comparison of Tables 4 and 5 shows that membrane deformation alters only mildly the  
678 process performances. Interestingly, the specific energy consumption decreases in all cases,  
679 while the apparent flux increases. The most affected configuration is that of case #5, where the  
680 specific energy consumption is found to be almost 2.50% lower than in the undeformed case.

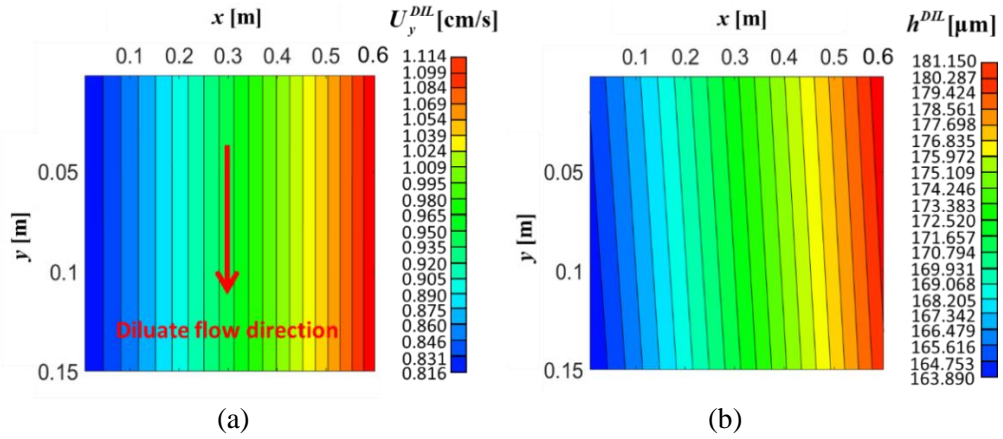
681 To better understand this behavior, for the sake of brevity, only diluate concentration and  
 682 current density maps of the second stack of case #5 are shown in Figure 8, comparing  
 683 undeformed and deformed channels, as these variables are the most affected by the membrane  
 684 deformation phenomena.



685  
 686

687 **Figure 8.** Maps of the diluate concentration  $C_{Bulk}^{DIL}$  (top row) and of the current density  $i_c$  (bottom row)  
 688 for the second cross-flow stack of case #5 without (a) and with (b) membrane deformation.

689 As can be seen in Figure 8, concentration and current density iso-lines are not straight any  
 690 more in the presence of deformation. In particular, iso-lines show a significant deflection close  
 691 to the channel outlet. To further investigate the reason of this behavior, maps of the diluate  
 692 superficial velocity along the main flow direction ( $y$ -axis) and of the equivalent channel height  
 693 in the presence of membrane deformation are shown in Figure 9.  
 694



695  
696

697 **Figure 9.** Maps of (a) diluate superficial velocity along the main flow direction (y-axis), and (b) channel  
698 height for the cross-flow case #5 in the presence of membrane deformation.

699 As it can be seen in Figure 9(a), the superficial velocity is 26.7% lower in the left side of  
700 the channel with respect to the right side, consistent with the distribution of the channel height,  
701 Figure 9(b), and thus of the hydraulic permeability. As a consequence, the residence time is  
702 higher in the left part of the stack compared to the right part. This favors the desalination process  
703 in the left side, so that local concentrations decrease more rapidly here along the flow direction  
704 y than in the right side, as shown in the top row of Figure 8(b). Moreover, the low-velocity area  
705 is larger than the high-velocity area, thus increasing the mean residence time. Note that the  
706 diluate channel is almost all compressed, and the average equivalent channel height is 172  $\mu\text{m}$ .

707

### 708 3.2.2 Heavy deformation effects

709 Based on the above results, it may be concluded that membrane deformation has negligible  
710 effects in ED applications for the geometry, membrane thickness  $t$  and membrane Young  
711 modulus  $E$  selected in this study (OCF  $P/H=8$ ,  $t=120 \mu\text{m}$ ,  $E=150 \text{ MPa}$ ). However, deformation  
712 effects might be larger for a different choice of these quantities.

713 In particular, treating either membrane portion included in a unit cell (Figure 2) as a non  
714 pre-stressed square flat membrane of side length  $2a$  subjected to a uniformly distributed load  
715  $q=\text{TMP}$ , having all edges clamped and undergoing large deflections, an approximate estimation  
716 of the deflection  $w_0$  at the center of the membrane surface is given by [54]:

$$717 \quad w_0 = f(\nu) \left( \frac{qa^4(1-\nu)}{Et} \right)^{1/3} \quad (34)$$

718 where  $\nu$  is the Poisson ratio and  $f(\nu) \approx 0.800 + 0.062\nu$ . For example, for membranes three  
719 times thinner than the above OCF ones, i.e. 40  $\mu\text{m}$ , or characterized by a Young modulus three  
720 times smaller, i.e. 50 MPa, any given deformation would be obtained under a load three times

721 smaller. Membranes with a thickness of 40  $\mu\text{m}$  or less represent a promising alternative in ED  
 722 and RED applications due to their lower electrical resistance [55].

723 In the light of these considerations, a preliminary investigation was carried out on the  
 724 effects of more severe membrane deformations than those considered in Section 3.2.1. To this  
 725 purpose, fictitious correlations for the channel hydraulic permeability ( $K$ ) and the equivalent  
 726 channel height ( $h^{SOL}$ ) as functions of TMP were built using the criterion that all effects caused  
 727 in the actual OCF membranes by a given TMP must occur in the fictitious membranes at  
 728 TMP/3. Table 6 reports the resulting correlations along with those for the actual OCF  
 729 membranes with  $t=120 \mu\text{m}$ ,  $E=150 \text{ MPa}$  considered so far. For the sake of simplicity, no change  
 730 was made in the correlations used to express the Sherwood numbers as functions of TMP, due  
 731 to the small influence of this quantity on the overall stack performance.

732

733 **Table 6.** Channel hydraulic permeability  $K$  and equivalent height  $h^{SOL}$  as functions of TMP for actual  
 734 and fictitious membranes. In the equations, TMP is in kPa.

	Actual membranes	Fictitious membranes
$K$ [m <sup>2</sup> ]	$2.4055 \cdot 10^{-13} \cdot \text{TMP}^2 - 3.4005 \cdot 10^{-11} \cdot \text{TMP} + 1.6560 \cdot 10^{-9}$	$2.27 \times 10^{-12} \times \text{TMP}^2 - 1.03 \times 10^{-10} \times \text{TMP} + 1.6560 \cdot 10^{-9}$
$h^{SOL}$ [m]	$6.00 \times 10^{-10} \times \text{TMP}^2 - 1.13 \times 10^{-6} \times \text{TMP} + 1.80 \times 10^{-4}$	$1.89 \times 10^{-9} \times \text{TMP}^3 - 7 \times 10^{-9} \times \text{TMP}^2 + -3.57 \times 10^{-6} \times \text{TMP} + 1.80 \times 10^{-4}$

735

736 Only results for *case #5*, which showed the highest membrane deformation effects among  
 737 the eight configuration studied in section 3.1, will be presented. Table 7 reports the same  
 738 quantities as Table 6 but comparing the cases of undeformed membranes, actual deformed  
 739 membranes (mild deformation), and fictitious deformed membranes (heavy deformation).

740

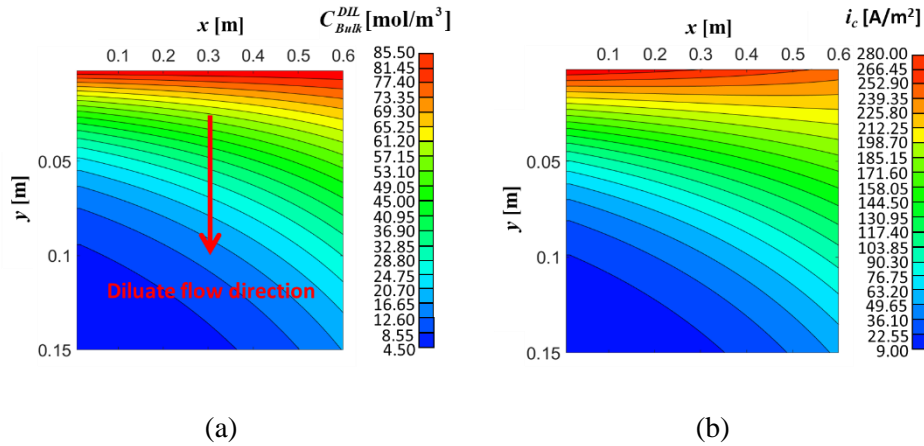
741 **Table 7.** Main results obtained for case #5 under the three conditions of no deformation, mild  
 742 deformation (actual OCF membranes) and heavy deformation (fictitious membranes).

Quantities	Undeformed	Mild Deformation	Heavy Deformation
$E_{spec}^{TOT}$ [kWh/m <sup>3</sup> ]	5.669	5.527	5.361
$J_p^{TOT}$ [l/m <sup>2</sup> h]	11.00	11.17	11.02
$I^1$ [A]	52.68	52.75	51.20
$I^2$ [A]	9.415	9.523	9.331
$V^1$ [V]	147.6	146.0	143.9
$V^2$ [V]	127.7	124.5	122.4

$h_{DIL}^1$ [ $\mu\text{m}$ ]	180.0	172.5	160.3
$h_{DIL}^2$ [ $\mu\text{m}$ ]	180.0	172.1	159.5
$R_{DIL}^1$ [ $\Omega$ ]	0.102	0.100	0.110
$R_{DIL}^2$ [ $\Omega$ ]	0.944	0.923	0.950
$Q_{TOT,OUTLET}^{DIL,2}$ [ $\text{l min}^{-1}$ ]	26.4	26.81	26.45

743

744 Results in Table 7 show that heavy membrane deformation conditions can influence the  
745 process' performances. Specifically, the total energy consumption decreases of more than 5%  
746 with respect to the undeformed case. The reason is the stronger redistribution of the fluid  
747 velocity with respect to the "mild deformation" case discussed in Section 3.2.1, as shown by  
748 the diluate concentration and current density maps in the second stack of case #5 reported in  
749 Figure 10. Note that in the heavy deformation case the diluate superficial velocity along the y-  
750 axis is more than twice higher in the right side of the channel than in the left side, thus strongly  
751 influencing the residence time. As a result, concentration and current density iso-lines are much  
752 more deflected than in the case of mild deformation of Figure 8. Table 7 shows also that the  
753 behavior of several quantities (among which  $J_p^{TOT}$ ) is not monotonic with the amplitude of the  
754 deformation.



755

756

757 **Figure 10.** Maps of diluate concentration  $C_{Bulk}^{DIL}$  (a) and current density  $i_c$  (b) for the second cross-flow  
758 stack of case #5 in the presence of heavy membrane deformation (compare with Figure 8).

759

## 760 Conclusions

761 In this paper, a novel 2-D, multi-scale, semi-empirical process model has been presented  
762 for the simulation of cross-flow Electrodeialysis (ED) systems in the presence and absence of

763 membrane deformation. The model is based on a multi-scale approach allowing the study of  
764 membrane deformation phenomena by exploiting results and modelling approaches of previous  
765 fluid-structure investigations performed by the authors. Specifically, at the lowest scale of a  
766 small repetitive unit of a fluid channel bounded by two profiled membranes, fluid dynamics  
767 and mass transport properties of deformed fluid channels have been taken into account using  
768 correlations previously determined by one-way coupled structural/fluid-dynamics simulations.  
769 At the higher scale of a whole channel dimension, an original previously developed two-way  
770 fluid-structure algorithm has been used to calculate the fluid, mass transfer characteristics and  
771 channel height redistribution in ED stacks considering the local membrane deformation.  
772 Finally, at the highest scale of an ED stack, all physical and electrochemical phenomena of the  
773 ED process have been computed to assess the performance of cross-flow ED stacks. In a first  
774 set of simulations without considering membrane deformation, the process performances of  
775 cross-flow ED stacks equipped with Overlapped Crossed Filaments (OCF) profiled membranes  
776 have been investigated for a two-stage desalination of seawater by changing the stack size and  
777 operating conditions. The use of shorter diluate channels increased the specific energy demand  
778 (due to a higher voltage) for a desalination process requiring, however, less membrane area and  
779 providing higher water recovery. Then, the same ED stack configurations have been simulated  
780 by including local membrane deformations. In this case, results have shown that membrane  
781 deformation did not affect significantly the process performances. In particular, the specific  
782 energy consumption decreased of ~2.5% in the most affected configuration with respect to its  
783 undeformed case. However, the use of thinner or less stiff membranes than the OCF ones  
784 (thickness lower than 120  $\mu\text{m}$  and Young modulus lower than 150 MPa) could lead to more  
785 severe membrane deformations and, thus, to larger effects on the process performance. In this  
786 regard, a preliminary investigation has shown that the specific energy consumption could  
787 decrease up to ~5% with respect to the undeformed case.

788 The paper presents a novel tool to support the design and the optimisation of cross-flow ED  
789 stacks and profiled membranes or spacers. Helpful information could be collected to guide  
790 membrane manufacturers and stack designers, especially in the early stages of the development  
791 of novel membranes or stacks.

792 Authors would also stress that, although the modelling tool has been presented for ED  
793 applications, the fundamental idea behind the simulation approach can be readily extended to  
794 the analysis of any other membrane-based process, where a differential pressure can generate  
795 local deformation of membranes and channels geometry.

796

797 **Acknowledgements**

798 This work was supported by the REvived water (Low energy solutions for drinking water  
799 production by a REvival of ElectroDialysis systems) project – Horizon 2020 programme, Grant  
800 Agreement no. 685579. The authors wish to thank REDstack for the experimental data  
801 provided.

802

803

804 **Appendix A: Correlations used for the physical and transport properties of NaCl**  
 805 **solutions.**

806 In the following appendix, the correlations for the physical and transport properties of NaCl  
 807 solutions used in the present model are reported. All the correlations (A.1-7) refer to a  
 808 temperature  $T_0$  of 25 °C and are taken by Annex 1 in [45].

- 809 • Solution density  $\rho^{SOL}$  (kg/m<sup>3</sup>):

810 
$$\rho^{SOL} = 5.94 \times 10^{-11} C^3 - 1.032 \times 10^{-6} C^2 + 4.097 \times 10^{-2} C + 997 \quad (A.1)$$

- 811 • Solution electrical conductivity  $\kappa^{SOL}$  (S/m):

812 
$$\log_{10}(\kappa^{SOL}) = -0.0027373(\log_{10}(C))^3 - 0.0059675(\log_{10}(C))^2 + \quad C \leq 1000 \quad (A.2)$$
  

$$+ 0.98994(\log_{10}(C)) - 1.9074$$

813 
$$\log_{10}(\kappa^{SOL}) = -1.3893(\log_{10}(C))^3 + 13.252(\log_{10}(C))^2 + \quad C \leq 1000 \quad (A.3)$$
  

$$- 41.277(\log_{10}(C)) + 43.011$$

- 814 • Salt diffusion  $D^{SOL}$  (m<sup>2</sup>/s):

815 
$$D^{SOL} = 1.47 \times 10^{-9} + 0.13 \times 10^{-9} e^{(-C/70)} \quad C \leq 400 \quad (A.4)$$

816 
$$D^{SOL} = -2.87262 \times 10^{-21} C^3 + 2.03219 \times 10^{-17} C^2 + \quad C > 400 \quad (A.5)$$
  

$$- 8.44113 \times 10^{-15} C + 1.4705 \times 10^{-9}$$

- 817 • Salt activity coefficients  $\gamma^{SOL}$  (dimensionless):

818 
$$\gamma^{SOL} = 0.64 + 0.189 e^{-C/260} + 0.1605 e^{-C/20} \quad C \leq 1200 \quad (A.6)$$

819 
$$\gamma^{SOL} = 0.64 + 0.189 e^{-C/260} + 0.1605 e^{-C/20} + 1.051 \times 10^{-7} (C - 1200)^{1.8} \quad C > 1200 \quad (A.7)$$

820 As discussed in Section 2.6, the temperature varied during the experiments used for model  
 821 validation from 18 to 22 °C. Therefore, empirical correlations for solution and membrane  
 822 resistances were employed to properly simulate the experimental conditions:

- 823 • Solution electrical conductivity as a function of the temperature (°C):

824 
$$\kappa^{SOL}(T) = \kappa^{SOL}(T_0) \frac{0.1692 \cdot T_0 + 4.7276}{0.1692 \cdot T + 4.7276} \quad (A.8)$$

- 825 • Membrane resistance as a function of the temperature (°C):

826 
$$R^{IEM}(T) = R^{IEM}(T_0) \frac{0.0023 \cdot T^2 - 0.1799 \cdot T + 5.1795}{0.0023 \cdot T_0^2 - 0.1799 \cdot T_0 + 5.1795} \quad (A.9)$$

827 Eqs. (A.8) and (A.9) were provided by the REDstack company.

828

829

830

831 **Appendix B: Correlations for membrane deformation**

832 In the following appendix correlations for hydraulic permeability, equivalent channel height,  
 833 volume porosity and Sherwood number as a function of TMP are reported. Correlations were  
 834 obtained for the OCF unit cell geometry of Figure 2 by performing computational fluid-structural  
 835 one-way simulations [29]. Note that in the correlations TMP is in kPa and positive value of  
 836 TMP causes the compression of a channel.

- 837 • Hydraulic channel permeability (m<sup>2</sup>):

$$838 \quad K = 2.40 \cdot 10^{-13} \cdot \text{TMP}^2 - 3.40 \cdot 10^{-11} \cdot \text{TMP} + 1.66 \cdot 10^{-9} \quad (\text{B.1})$$

- 839 • Unit cell fluid volume (mm<sup>3</sup>):

$$840 \quad V_f = 1.53 \cdot 10^{-6} \cdot \text{TMP}^2 - 2.89 \cdot 10^{-3} \cdot \text{TMP} + 0.46 \quad (\text{B.2})$$

- 841 • Equivalent channel height, in μm, calculated as the unit cell fluid volume over the cell  
 842 projected area (2.56 mm<sup>2</sup>):

$$843 \quad h^{SO_L} = 6.00 \times 10^{-4} \times \text{TMP}^2 - 1.13 \times \text{TMP} + 180 \quad (\text{B.3})$$

- 844 • Channel porosity calculated as the ratio between unit cell fluid volume over total cell  
 845 volume of the undeformed channel without profiles (0.512 mm<sup>3</sup>):

$$846 \quad \varepsilon = 3.00 \cdot 10^{-6} \cdot \text{TMP}^2 - 5.64 \cdot 10^{-3} \cdot \text{TMP} + 0.90 \quad (\text{B.4})$$

- 847 • Sherwood number (Sh) from [29] considering a fluid flow attack angle of 45°:

- 848 • TMP=0

$$849 \quad \text{Sh} = 0.346 \times \ln(\text{Re}) + 9.552; \quad (\text{Re} \leq 17.5) \quad (\text{B.5})$$

$$850 \quad \text{Sh} = 5.314 \times \ln(\text{Re}) - 4.636; \quad (\text{Re} > 17.5) \quad (\text{B.6})$$

- 851 • TMP=10 kPa

$$852 \quad \text{Sh} = 0.414 \times \ln(\text{Re}) + 10.121; \quad (\text{Re} \leq 14.3) \quad (\text{B.7})$$

$$853 \quad \text{Sh} = 4.498 \times \ln(\text{Re}) - 0.723; \quad (\text{Re} > 14.3) \quad (\text{B.8})$$

- 854 • TMP=20 kPa

$$855 \quad \text{Sh} = 0.417 \times \ln(\text{Re}) + 11.072; \quad (\text{Re} \leq 11.52) \quad (\text{B.9})$$

$$856 \quad \text{Sh} = 3.906 \times \ln(\text{Re}) + 2.616; \quad (\text{Re} > 11.52) \quad (\text{B.10})$$

- 857 • TMP=30 kPa

$$858 \quad \text{Sh} = 0.462 \times \ln(\text{Re}) + 11.685; \quad (\text{Re} \leq 9.2) \quad (\text{B.11})$$

$$859 \quad \text{Sh} = 2.750 \times \ln(\text{Re}) + 6.615; \quad (\text{Re} > 9.2) \quad (\text{B.12})$$

- 860 • TMP=-10 kPa

$$861 \quad \text{Sh} = 0.440 \times \ln(\text{Re}) + 8.934; \quad (\text{Re} \leq 21.3) \quad (\text{B.13})$$

$$862 \quad \text{Sh} = 6.608 \times \ln(\text{Re}) - 9.812; \quad (\text{Re} > 21.3) \quad (\text{B.14})$$



874 NOMENCLATURE

$C^{DIL}, C^{CON}, C^{SOL}$	Concentration of <i>DIL</i> , <i>CON</i> or generic <i>SOL</i> ( <i>DIL</i> or <i>CON</i> ) solutions	mol/m <sup>3</sup>
$C_{Bulk}^{SOL}, C_{IEM}^{SOL}$	Concentration in the bulk of a generic solution <i>SOL</i> and at the a generic membrane <i>IEM</i> -solution interface	mol/m <sup>3</sup>
$D^{IEM}, D^{SOL}$	Salt diffusivity in a generic <i>IEM</i> and solution <i>SOL</i>	m <sup>2</sup> /s
$E_{spec}$	Energy consumption per unit volume of product	kWh/m <sup>3</sup>
$F$	Faraday constant (96,485)	C/mol
$H$	Undeformed nominal channel thicknesses	m
$h^{SOL}$	Equivalent fluid channel thickness of a generic solution <i>SOL</i>	m
$I$	Overall stack electric current	A
$i_c$	Ionic current density	A/m <sup>2</sup>
$N_{SALT}^{TOT}, N_{Coul}^{TOT}, N_{Diff}^{TOT}$	Total, Coulombic and diffusive salt fluxes	mol/(m <sup>2</sup> s)
$J_p$	Apparent product flux	l/(m <sup>2</sup> h)
$J_W^{TOT}, J_W^{E.OSM}, J_W^{OSM}$	Total, osmotic and electro-osmotic water fluxes	m <sup>3</sup> /(m <sup>2</sup> s)
$K$	Channel hydraulic permeability	m <sup>2</sup>
$L$	Fluid channel length	m
$L_{p,IEM}$	Water permeability coefficient of a generic <i>IEM</i>	ml/(m <sup>2</sup> hbar)
$M_w$	Water molecular weight	kg/mol
$N_{Block}^x, N_{Block}^y$	Number of rectangular blocks	-
$N_{cp}$	Total number of cell pairs	-
$n_h$	Hydration number	-
$P$	Profiled membrane pitch	m
$P_{el}, P_{pump}$	Electric and pumping power consumption	W
$Q^{CON}, Q^{DIL}$	<i>CON</i> and <i>DIL</i> solution flow rates	m <sup>3</sup> /s
$Q_{TOT,av}^{CON}, Q_{TOT,av}^{DIL}$	Average overall (stack) <i>CON</i> and <i>DIL</i> solution flow rates	m <sup>3</sup> /s
$Q_{TOT,OUTLET}^{DIL}$	Overall diluate outlet flow rate	m <sup>3</sup> /s
$R$	Universal gas constant (8.314)	J/(mol K)
$R^{CON}, R^{DIL}, R^{SOL}$	Areal resistance of <i>CON</i> , <i>DIL</i> and generic <i>SOL</i> solutions	Ω m <sup>2</sup>
$R^{CEM}, R^{AEM}, R^{IEM}$	Areal resistance of <i>CEM</i> , <i>AEM</i> and generic <i>IEM</i> membranes	Ω m <sup>2</sup>
$R_{TOT}, R_{blank}$	Total areal resistance of a cell pair and electrode compartments	Ω m <sup>2</sup>
Re	Reynolds number	-
Sh	Sherwood number	-
$T$	Temperature	K
$t$	Membrane thickness	m
$U_x^{SOL}, U_y^{SOL}$	Superficial velocities along <i>x</i> and <i>y</i> in the channel <i>SOL</i>	m/s
$V_f$	Volume of fluid channels	m <sup>3</sup>

$V, V_{cp}$	Potential voltage drop applied by a power supply and voltage drop over a cell pair	V
$v_c, v_d$	Inlet velocities of the <i>CON</i> and <i>DIL</i> solutions	m/s
$W$	Fluid channel width	m
$x$	Component of Cartesian coordinate system	m
$y$	Component of Cartesian coordinate system	m

875

## 876 Greek symbols

$\alpha_{IEM}$	Perm-selectivity of a generic <i>IEM</i>	-
$\gamma^{CON}, \gamma^{DIL}$	Salt activity coefficients in <i>CON</i> and <i>DIL</i> solutions	-
$\varepsilon$	Channel porosity	-
$\eta, \eta_{BL}, \eta_{IEM}^{SOL}$	Total non-Ohmic voltage drop, non-Ohmic voltage drop due to concentration polarization and voltage drop at each <i>SOL/IEM</i> interface	V
$\theta_{IEM}^{SOL}$	Polarization coefficient at the generic <i>SOL/IEM</i> interface	-
$\kappa^{SOL}$	Electrical conductivity of the generic <i>SOL</i>	S/m
$\mu$	Fluid viscosity	Pa s
$\pi_{IEM}^{SOL}$	Osmotic pressure at the at the generic <i>SOL/IEM</i> interface	Pa
$\rho^{SOL}, \rho_w$	<i>SOL</i> and water density	kg/m <sup>3</sup>
$\varphi$	Non-ohmic voltage drop due to fluid concentration gradient	V
$\Delta x, \Delta y$	Length and width of rectangular blocks	m
$\Delta p^{CON}, \Delta p^{DIL}$	Pressure drops in the <i>CON</i> and <i>DIL</i> channels	Pa

877

## 878 Acronyms and abbreviations

AEM	Anion Exchange membranes
BL	Boundary Layer
Blank	Electrode compartments
CEM	Cation Exchange Membranes
CFD	Computational fluid dynamics
CON	Concentrate solution
CP	Cell pair
DIL	Diluate solution
ED	Electrodialysis
FE	Finite Element Method
FV	Finite Volume Method
IEM	Generic Ion Exchange Membrane (AEM or CEM)
RED	Reverse Electrodialysis
SOL	Generic Solution (CON or DIL)
TMP	Transmembrane pressure

879

## References

- [1] M. Qasim, M. Badrelzaman, N.N. Darwish, N.A. Darwish, N. Hilal, Reverse osmosis desalination: A state-of-the-art review, *Desalination*. 459 (2019) 59–104. <https://doi.org/10.1016/j.desal.2019.02.008>.
- [2] A. Campione, L. Gurreri, M. Ciofalo, G. Micale, A. Tamburini, A. Cipollina, Electrodialysis for water desalination: A critical assessment of recent developments on process fundamentals, models and applications, *Desalination*. 434 (2018) 121–160. <https://doi.org/10.1016/J.DESAL.2017.12.044>.
- [3] P.S. Goh, T.W. Wong, J.W. Lim, A.F. Ismail, N. Hilal, Innovative and sustainable membrane technology for wastewater treatment and desalination application, in: *Innov. Strateg. Environ. Sci.*, Elsevier, 2020: pp. 291–319. <https://www.sciencedirect.com/science/article/pii/B9780128173824000095>.
- [4] L. Gurreri, A. Tamburini, A. Cipollina, G. Micale, Electrodialysis Applications in Wastewater Treatment for Environmental Protection and Resources Recovery: A Systematic Review on Progress and Perspectives, *Membranes (Basel)*. 10 (2020) 146. <https://doi.org/10.3390/membranes10070146>.
- [5] M. Bdiri, L. Dammak, C. Larchet, F. Hellal, M. Porozhnyy, E. Nevakshenova, N. Pismenskaya, V. Nikonenko, Characterization and cleaning of anion-exchange membranes used in electrodialysis of polyphenol-containing food industry solutions; comparison with cation-exchange membranes, *Sep. Purif. Technol.* 210 (2019) 636–650. <https://doi.org/10.1016/J.SEPPUR.2018.08.044>.
- [6] Y. Cui, X.Y. Liu, T.S. Chung, Enhanced osmotic energy generation from salinity gradients by modifying thin film composite membranes, *Chem. Eng. J.* 242 (2014) 195–203. <https://doi.org/10.1016/j.cej.2013.12.078>.
- [7] M. Tedesco, A. Cipollina, A. Tamburini, G. Micale, Towards 1 kW power production in a reverse electrodialysis pilot plant with saline waters and concentrated brines, *J. Memb. Sci.* 522 (2017) 226–236. <https://doi.org/10.1016/J.MEMSCI.2016.09.015>.
- [8] D.F. Stamatialis, B.J. Papenburg, M. Gironés, S. Saiful, S.N.M. Bettahalli, S. Schmitmeier, M. Wessling, Medical applications of membranes: Drug delivery, artificial organs and tissue engineering, *J. Memb. Sci.* 308 (2008) 1–34. <https://doi.org/https://doi.org/10.1016/j.memsci.2007.09.059>.
- [9] R.W. Baker, *Membrane Technology and Applications*, John Wiley & Sons, 2004.
- [10] D.A. Ladner, A. Subramani, M. Kumar, S.S. Adham, M.M. Clark, Bench-scale evaluation of seawater desalination by reverse osmosis, *Desalination*. 250 (2010) 490–499. <https://doi.org/10.1016/j.desal.2009.06.072>.
- [11] A.J. Charlton, B. Lian, G. Blandin, G. Leslie, P. Le-Clech, Impact of FO operating pressure and membrane tensile strength on draw-channel geometry and resulting hydrodynamics, *Membranes (Basel)*. 10, 111 (2020). <https://doi.org/10.3390/membranes10050111>.
- [12] G. Blandin, A.R.D. Verliefde, C.Y. Tang, A.E. Childress, P. Le-Clech, Validation of assisted forward osmosis (AFO) process: Impact of hydraulic pressure, *J. Memb. Sci.* 447 (2013) 1–11. <https://doi.org/10.1016/j.memsci.2013.06.002>.
- [13] H.T. Madsen, S.S. Nissen, J. Muff, E.G. Sjøgaard, Pressure retarded osmosis from hypersaline solutions: Investigating commercial FO membranes at high pressures, *Desalination*. 420 (2017) 183–190. <https://doi.org/10.1016/j.desal.2017.06.028>.

- [14] K.L. Hickenbottom, J. Vanneste, M. Elimelech, T.Y. Cath, Assessing the current state of commercially available membranes and spacers for energy production with pressure retarded osmosis, *Desalination*. 389 (2016) 108–118. <https://doi.org/10.1016/j.desal.2015.09.029>.
- [15] G. Han, S. Zhang, X. Li, T.S. Chung, Progress in pressure retarded osmosis (PRO) membranes for osmotic power generation, *Prog. Polym. Sci.* 51 (2014) 1–27. <https://doi.org/10.1016/j.progpolymsci.2015.04.005>.
- [16] A.P. Straub, N.Y. Yip, M. Elimelech, Raising the Bar: Increased Hydraulic Pressure Allows Unprecedented High Power Densities in Pressure-Retarded Osmosis, *Environ. Sci. Technol. Lett.* 1 (2014) 55–59. <https://doi.org/10.1021/ez400117d>.
- [17] Q. She, X. Jin, C.Y. Tang, Osmotic power production from salinity gradient resource by pressure retarded osmosis: Effects of operating conditions and reverse solute diffusion, *J. Memb. Sci.* 401–402 (2012) 262–273. <https://doi.org/10.1016/J.MEMSCI.2012.02.014>.
- [18] Q. She, D. Hou, J. Liu, K.H. Tan, C.Y. Tang, Effect of feed spacer induced membrane deformation on the performance of pressure retarded osmosis (PRO): Implications for PRO process operation, *J. Memb. Sci.* 445 (2013) 170–182. <https://doi.org/10.1016/j.memsci.2013.05.061>.
- [19] W. Gai, X. Li, J.Y. Xiong, C.F. Wan, T.S. Chung, Evolution of micro-deformation in inner-selective thin film composite hollow fiber membranes and its implications for osmotic power generation, *J. Memb. Sci.* 516 (2016) 104–112. <https://doi.org/10.1016/j.memsci.2016.06.007>.
- [20] Y.C. Kim, M. Elimelech, Adverse impact of feed channel spacers on the performance of pressure retarded osmosis, *Environ. Sci. Technol.* 46 (2012) 4673–4681. <https://doi.org/10.1021/es3002597>.
- [21] X. Li, S. Zhang, F. Fu, T.S. Chung, Deformation and reinforcement of thin-film composite (TFC) polyamide-imide (PAI) membranes for osmotic power generation, *J. Memb. Sci.* 434 (2013) 204–217. <https://doi.org/10.1016/j.memsci.2013.01.049>.
- [22] Z. Yuan, L. Wei, J.D. Afroz, K. Goh, Y. Chen, Y. Yu, Q. She, Y. Chen, Pressure-retarded membrane distillation for low-grade heat recovery: The critical roles of pressure-induced membrane deformation, *J. Memb. Sci.* 579 (2019) 90–101. <https://doi.org/10.1016/j.memsci.2019.02.045>.
- [23] F. Mahmoudi, A. Date, A. Akbarzadeh, Further investigation of simultaneous fresh water production and power generation concept by permeate gap membrane distillation system, *J. Memb. Sci.* 572 (2019) 230–245. <https://doi.org/10.1016/j.memsci.2018.11.004>.
- [24] S.-M. Huang, Laminar flow and heat transfer in plate membrane channels: Effects of the deformation heights, *Int. J. Therm. Sci.* 109 (2016) 44–53. <https://doi.org/10.1016/J.IJTHEMALSCI.2016.05.032>.
- [25] Y. Zhou, K. Jiao, Q. Du, Y. Yin, X. Li, Gas diffusion layer deformation and its effect on the transport characteristics and performance of proton exchange membrane fuel cell, *Int. J. Hydrogen Energy*. 38 (2013) 12891–12903. <https://doi.org/10.1016/J.IJHYDENE.2013.05.150>.
- [26] Z. Shi, X. Wang, A numerical study of flow crossover between adjacent flow channels in a proton exchange membrane fuel cell with serpentine flow field, *J. Power Sources*. 185 (2008) 985–992. <https://doi.org/10.1016/J.JPOWSOUR.2008.09.008>.

- [27] Q.B. Chen, J. Wang, Y. Liu, J. Zhao, P. Li, Novel energy-efficient electro dialysis system for continuous brackish water desalination: Innovative stack configurations and optimal inflow modes, *Water Res.* 179 (2020) 115847. <https://doi.org/10.1016/j.watres.2020.115847>.
- [28] M. Yasukawa, S. Mehdizadeh, T. Sakurada, T. Abo, M. Kuno, M. Higa, Power generation performance of a bench-scale reverse electro dialysis stack using wastewater discharged from sewage treatment and seawater reverse osmosis, *Desalination.* 491 (2020) 114449. <https://doi.org/10.1016/j.desal.2020.114449>.
- [29] G. Battaglia, L. Gurreri, G. Airòfarulla, A. Cipollina, A. Pirrotta, G. Micale, M. Ciofalo, Membrane deformation and its effects on flow and mass transfer in the electromembrane processes, *Int. J. Mol. Sci.* 20 (2019). <https://doi.org/10.3390/ijms20081840>.
- [30] G. Battaglia, L. Gurreri, G.A. Farulla, A. Cipollina, A. Pirrotta, G. Micale, M. Ciofalo, Pressure-induced deformation of pillar-type profiled membranes and its effects on flow and mass transfer, *Computation.* 7 (2019). <https://doi.org/10.3390/computation7020032>.
- [31] G. Battaglia, L. Gurreri, A. Cipollina, A. Pirrotta, S. Velizarov, M. Ciofalo, G. Micale, Fluid-structure interaction and flow redistribution in membrane-bounded channels, *Energies.* 12 (2019). <https://doi.org/10.3390/en12224259>.
- [32] H. Strathmann, Electro dialysis, a mature technology with a multitude of new applications, *Desalination.* 264 (2010) 268–288. <https://doi.org/10.1016/J.DESAL.2010.04.069>.
- [33] M. Sadrzadeh, A. Kaviani, T. Mohammadi, Mathematical modeling of desalination by electro dialysis, *Desalination.* 206 (2007) 538–546. <https://doi.org/10.1016/J.DESAL.2006.04.062>.
- [34] H.-J. Lee, F. Sarfert, H. Strathmann, S.-H. Moon, Designing of an electro dialysis desalination plant, *Desalination.* 142 (2002) 267–286. [https://doi.org/10.1016/S0011-9164\(02\)00208-4](https://doi.org/10.1016/S0011-9164(02)00208-4).
- [35] J.A. Wesselingh, P. Vonk, G. Kraaijeveld, Exploring the Maxwell-Stefan description of ion exchange, *Chem. Eng. J. Biochem. Eng. J.* 57 (1995) 75–89. [https://doi.org/10.1016/0923-0467\(94\)02932-6](https://doi.org/10.1016/0923-0467(94)02932-6).
- [36] Z. Zourmand, F. Faridirad, N. Kasiri, T. Mohammadi, Mass transfer modeling of desalination through an electro dialysis cell, *Desalination.* 359 (2015) 41–51. <https://doi.org/10.1016/J.DESAL.2014.12.008>.
- [37] M. Tedesco, H.V.M. Hamelers, P.M. Biesheuvel, Nernst-Planck transport theory for (reverse) electro dialysis: I. Effect of co-ion transport through the membranes, *J. Memb. Sci.* 510 (2016) 370–381. <https://doi.org/10.1016/J.MEMSCI.2016.03.012>.
- [38] L. Gurreri, G. Battaglia, A. Tamburini, A. Cipollina, G. Micale, M. Ciofalo, Multi-physical modelling of reverse electro dialysis, *Desalination.* 423 (2017) 52–64. <https://doi.org/10.1016/J.DESAL.2017.09.006>.
- [39] M.M. Generous, N.A.A.A. Qasem, S.M. Zubair, The significance of modeling electro dialysis desalination using multi-component saline water, *Desalination.* (2020) 114347. <https://doi.org/https://doi.org/10.1016/j.desal.2020.114347>.
- [40] N.C. Wright, S.R. Shah, S.E. Amrose, A.G. Winter, A robust model of brackish water electro dialysis desalination with experimental comparison at different size scales, *Desalination.* 443 (2018) 27–43. <https://doi.org/10.1016/J.DESAL.2018.04.018>.

- [41] M. Fidaleo, M. Moresi, Optimal strategy to model the electrodialytic recovery of a strong electrolyte, *J. Memb. Sci.* 260 (2005) 90–111. <https://doi.org/10.1016/J.MEMSCI.2005.01.048>.
- [42] R.K. McGovern, S.M. Zubair, J.H. Lienhard V, The cost effectiveness of electro dialysis for diverse salinity applications, *Desalination*. 348 (2014) 57–65. <https://doi.org/10.1016/j.desal.2014.06.010>.
- [43] S.R. Shah, N.C. Wright, P.A. Nepsky, A.G. Winter, Cost-optimal design of a batch electro dialysis system for domestic desalination of brackish groundwater, *Desalination*. 443 (2018) 198–211. <https://doi.org/10.1016/J.DESAL.2018.05.010>.
- [44] S. Pawlowski, V. Geraldes, J.G. Crespo, S. Velizarov, Computational fluid dynamics (CFD) assisted analysis of profiled membranes performance in reverse electro dialysis, *J. Memb. Sci.* 502 (2016) 179–190. <https://doi.org/10.1016/J.MEMSCI.2015.11.031>.
- [45] M. La Cerva, M. Di Liberto, L. Gurreri, A. Tamburini, A. Cipollina, G. Micale, M. Ciofalo, Coupling CFD with a one-dimensional model to predict the performance of reverse electro dialysis stacks, *J. Memb. Sci.* 541 (2017) 595–610. <https://doi.org/10.1016/J.MEMSCI.2017.07.030>.
- [46] A. Campione, A. Cipollina, I.D.L. Bogle, L. Gurreri, A. Tamburini, M. Tedesco, G. Micale, A hierarchical model for novel schemes of electro dialysis desalination, *Desalination*. 465 (2019) 79–93. <https://doi.org/10.1016/J.DESAL.2019.04.020>.
- [47] A. Culcasi, L. Gurreri, A. Zaffora, A. Cosenza, A. Tamburini, A. Cipollina, G. Micale, Ionic shortcut currents via manifolds in reverse electro dialysis stacks, *Desalination*. 485 (2020). <https://doi.org/10.1016/j.desal.2020.114450>.
- [48] A. Culcasi, L. Gurreri, A. Zaffora, A. Cosenza, A. Tamburini, G. Micale, On the modelling of an Acid/Base Flow Battery: An innovative electrical energy storage device based on pH and salinity gradients, *Appl. Energy*. 277 (2020). <https://doi.org/10.1016/j.apenergy.2020.115576>.
- [49] M. Tedesco, P. Mazzola, A. Tamburini, G. Micale, I.D.L. Bogle, M. Papapetrou, A. Cipollina, Analysis and simulation of scale-up potentials in reverse electro dialysis, *Desalin. Water Treat.* 55 (2015) 3391–3403. <https://doi.org/10.1080/19443994.2014.947781>.
- [50] C. Simões, D. Pintossi, M. Saakes, Z. Borneman, W. Brillman, K. Nijmeijer, Electrode segmentation in reverse electro dialysis: Improved power and energy efficiency, *Desalination*. 492 (2020). <https://doi.org/10.1016/j.desal.2020.114604>.
- [51] A.H. Galama, N.A. Hoog, D.R. Yntema, Method for determining ion exchange membrane resistance for electro dialysis systems, *Desalination*. 380 (2016) 1–11. <https://doi.org/10.1016/J.DESAL.2015.11.018>.
- [52] M. La Cerva, L. Gurreri, M. Tedesco, A. Cipollina, M. Ciofalo, A. Tamburini, G. Micale, Determination of limiting current density and current efficiency in electro dialysis units, *Desalination*. 445 (2018) 138–148. <https://doi.org/10.1016/j.desal.2018.07.028>.
- [53] M. La Cerva, L. Gurreri, A. Cipollina, A. Tamburini, M. Ciofalo, G. Micale, Modelling and cost analysis of hybrid systems for seawater desalination: Electromembrane pre-treatments for Reverse Osmosis, *Desalination*. 467 (2019) 175–195. <https://doi.org/10.1016/j.desal.2019.06.010>.
- [54] J.J. Vlassak, W.D. Nix, A new bulge test technique for the determination of Young's modulus and Poisson's ratio of thin films, *J. Mater. Res.* 7 (1992) 3242–3249.

<https://doi.org/10.1557/JMR.1992.3242>.

- [55] M. Tedesco, H.V.M. Hamelers, P.M. Biesheuvel, Nernst-Planck transport theory for (reverse) electro dialysis: III. Optimal membrane thickness for enhanced process performance, *J. Memb. Sci.* 565 (2018) 480–487.  
<https://doi.org/10.1016/J.MEMSCI.2018.07.090>.